Optical Materials 89 (2019) 48–62

Contents lists available at ScienceDirect

Optical Materials

journal homepage: www.elsevier.com/locate/optmat

Vibrational spectra, dielectric properties, conductivity mechanisms and third order nonlinear optical properties of guanidinium 4-aminobenzoate

Jesby George[a], V. Sasikala[a], Lija K. Joy[a], D. Sajan[a,*], T. Arumanayagam[b], P. Murugakoothan[b], G. Vinitha[c]

[a] Centre for Advanced Functional Materials, Post Graduate & Research Department of Physics, Bishop Moore College, Mavelikara, Kerala, 690 110, India
[b] Post Graduate & Research Department of Physics, Pachaiyappa's College, Chennai, 600 030, India
[c] Division of Physics, School of Advanced Sciences, Vellore Institute of Technology (VIT), Chennai, 600127, India

ARTICLE INFO

Keywords:
Cole-Cole plot
Electron-hole transport
NLO
Z-scan
Hyperpolarizability

ABSTRACT

The frequency response of dielectric permittivity measurements at temperatures 35 °C and 100 °C suggests enhanced inherent optical quality and few defects in the crystal. The Cole-Cole plot shows the presence of grain and grain boundary, it is found that single relaxation is observed in the crystal. The ac and dc conductivity and dielectric behavior of the grown crystal were systemically investigated as a function of frequency and temperature. The third order nonlinear optical property extensively studied by z-scan technique revealed high third order nonlinearity in the form of self-defocusing and two-photon absorption with saturable absorption. The strong intermolecular charge transfer interaction evident from NBO and AIM studies confirms the NLO property of the material. The detailed vibrational assignments were carried out on the basis of potential energy distribution (PED) analysis and scaled quantum mechanical force field calculation using MOLVIB program. The red shifted NH stretching wavenumbers and the broadening of corresponding bands in the solid state as well as the gas phase spectra, optimized molecular geometry and NBO analysis have confirmed the presence of N-H···O hydrogen bonding in G4AB.

1. Introduction

Organic derivatives comprising of molecules with strong electron donor and acceptor groups are well known to exhibit significant nonlinear optical (NLO) activities due to their electron transfer mechanisms by the intramolecular charge transfer interaction (ICT) processes that are mediated by the push-pull substituent pairs which cause large hyperpolarizabilities to the molecular systems [1]. The extended hydrogen bonding associations can result in the structural asymmetry of the molecular system which is an important requirement for the materials to have NLO applications [2]. Crystallization of ionic salt produce can more cohesive crystalline structures which possess inherently greater thermal stabilities, sufficient mechanical strength and have higher chromophore number densities which are requisites for quadratic NLO effects [3].

The organic complexes of cationic guanidinium based systems have received considerable attention as NLO materials [3–7] due to their capability to form multiple, strong and charge assisted hydrogen bonds with the carboxylate group, phosphate group, nitrate group and polar molecules [8]. The guanidinium cation is formed by the protonation on guanidine which is a strong organic base and the cation is stabilized through the Y-aromaticity by the delocalization of positive charge on the three nitrogen atoms and the central carbon atom within the CN_3 unit. The concept of aromatic domino effect stresses the importance of the aromatic stabilization triggered by protonation [9–15]. 4-aminobenzoic acid is one of the most versatile of the carboxylic acids for co-crystal formation. The acid molecules have the property of establishing molecular self-assembly by extended hydrogen bonding structures through both the carboxylic acid group and the ring-substituted amino group with other molecules and thereby promoting stability to the resulting crystalline structure [16]. The molecular complexes of 4-aminobenzoic acid such as, the coordination polymer $[Zn(C_7H_7NO_2)_2]\cdot H_2O$ [10], Morpholin-4-ium p-aminobenzoate [17] and 2-amino-4-picolinium 4-aminobenzoate [18] have been identified as potential NLO materials. The surface-enhanced Raman spectroscopy of p-aminobenzoic acid with excitation in the visible and near infrared spectral region has been reported by *E.J. Liang* et al. [19]. The growth and physico-chemical properties of gunidinium derivatives such as Guanidinium tetrafluoroborate [20], Guanidinium trichloroacetate [21], Guanidinium 3-nirobenzoate [22] and Guanidinium tosylate [23] have

* Corresponding author.
E-mail addresses: drsajanbmc@gmail.com, dsajanbmc@gmail.com (D. Sajan).

https://doi.org/10.1016/j.optmat.2019.01.006
Received 18 October 2018; Received in revised form 19 December 2018; Accepted 9 January 2019
0925-3467/ © 2019 Elsevier B.V. All rights reserved.

been recently reported. The molecular structure and vibrational spectral studies of the derivatives of guanidinium [24–29] and the complexes of 4-aminobenzoate [30,31] have been extensively studied using quantum chemical density functional theory (DFT) calculations in recent years. The present work deals with the dielectric, third order NLO property and vibrational spectral studies of Guanidinium 4-amino benzoate (G4AB) crystal based on FT-IR and FT-Raman spectra along with DFT theoretical support to elucidate the relationship between the molecular structural features and NLO properties.

2. Experimental methods

Powder X-ray diffraction pattern measured by the Rigaku MinFlex 600, table top XRD diffractometer (Bragg-Brentano geometry) operated at 40 kV and 15 mA with monochromated Cu Ka radiation (λ = 1.5406 Å). The FT-IR and FT-Raman spectra of the sample were recorded with the Perkin Elmer spectrometer using the KBr pellet technique in the range 4000–400 cm^{-1} and with the Perkin Elmer GX 2000 FT-Raman spectrometer in the range 4000–50 cm^{-1}, respectively. The optical properties of the grown crystals were characterized by UV-Vis-NIR spectroscopy and the absorption spectrum was recorded using the Shimadzu 1061 UV-Vis-NIR spectrophotometer in the region 190-1100 nm. A single crystal of G4AB with dimensions 7.73 mm × 6.78 mm × 2.50 mm was used for the dielectric measurements. The dielectric parameters such as capacitance and dielectric loss were measured at two temperatures (35 °C and 100 °C) as a function of frequencies in the range 5Hz-5MHz with the instrument Hiocki 3532-50 LCR HiTESTER.

3. Computational methods

The molecular geometry optimization, static and dynamic first-hyperpolarizabilities and natural bond orbital (NBO) analysis [32] for isolated gas phase G4AB molecule in the ground state were calculated with density functional theory using B3LYP/6-311G(d) [29,30] level of theory with the aid of Gaussian 09 program [35]. The detailed vibrational assignments for the theoretical vibrational spectra of G4AB were carried out on the basis of potential energy distribution (PED) analysis using MOLVIB 7.0 program [36]. The vibrational wavenumbers calculated by B3LYP/6-311G(d) method were scaled using the scaled quantum mechanical force field (SQMFF) [37,38] method and were compared with the experimental FT-IR and FT-Raman spectra. The TD-DFT/B3LYP/6-311G(d) method was employed to simulate the theoretical electron absorption spectra at the gas and the water phases for G4AB. Atoms in Molecule (AIM) theory provides deep understanding of hydrogen bonding interactions from the topological parameters such as electron density ρ(r), Laplacian of electron density ρ(r) using AIMALL program [34,39].

4. Results and discussions

4.1. Synthesis and crystal growth

The salt of guanidinium 4-aminobenzoate is synthesized by mixing 0.5 mol of guanidine carbonate in 50 mL of deionized water; the prepared solution is then mixed with 1 mol of 4-aminobenzoic acid dissolved in 50 mL of methanol. The mixture of the solutions is stirred continuously for 2 h at a temperature of 50 °C. The filtered saturated solution is then allowed for slow evaporation.

The purity of the synthesized salt is improved by successive recrystallization with 1:1 water-methanol solvent [40]. The prepared solution is then allowed for crystal formation by slow evaporation growth method. Good quality single crystals of G4AB were collected after a period of two weeks as shown in Fig. 1.

Solubility study has been carried out using a constant temperature bath, controlled with an accuracy of ± 0.01 °C. The solubility of G4AB in water and water-methanol (1:1) solvents has been determined for the temperature range 30–50 °C by the gravimetrical method. The solubility of G4AB as a function of temperature is depicted in Fig. 2(a) which shows that the solubility is higher in water-methanol mixed solvent with positive slope.

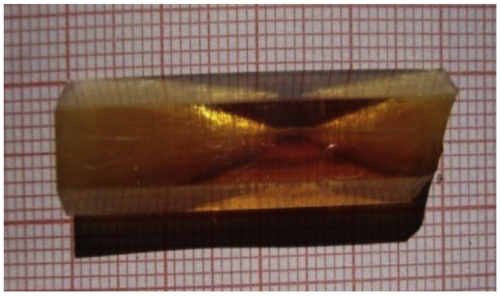

Fig. 1. Grown crystal of G4AB.

The conventional polythermal method was employed to measure the metastable zone width. The prepared solution was preheated to 5 °C above its saturated temperature and filtered with a fine filter paper. The saturated solution was gradually cooled from the preheated temperature until the first visible crystal could be observed. The temperature at which the first speck of a particle appeared was noted as nucleation temperature. The difference in temperature between the saturated temperature and the nucleation temperature is regarded as the metastable zone width of the sample. The metastable zone width of G4AB single crystal is given in Fig. 2(b). From the graph it is clear that the metastable zone width decrease with increase of saturation temperature.

Comparison between the PXRD patterns of the grown crystals of G4AB with the simulated single crystal XRD spectral patterns are shown in Fig. 3. The experimental diffractogram confirms the synthesis and crystallization of G4AB. Some peaks with high intensity in the experimental diffractogram (for example (121) and (134)) but with very low intensity in the simulated, this discrepancies are due to preferred orientation effects. The well-defined high intensity sharp peaks in the PXRD pattern confirmed that the grown sample is in good crystalline nature.

4.2. Dielectric properties

The frequency response of dielectric permittivity measurements of G4AB crystal at temperatures 35 °C and 100 °C were carried out. The variation of real (ε') and imaginary (ε") dielectric constants and dielectric loss (tan(δ)) with respect to frequency and temperatures are respectively shown in Fig. 4. It is noticed that the value of dielectric permittivity of the samples decreases with increase in frequency. This is the normal dielectric behavior and can be interpreted on the basis of polarization mechanisms such as atomic polarization of lattice, space charge polarization, orientation polarization of dipoles, electronic and ionic polarization [41]. At higher frequencies the dipoles are unable to respond promptly to follow the applied field and consequently the dipole polarization decreases and leads to smaller dielectric values. Due to the ionic mobility, the dielectric loss shows larger values in lower frequency region. The low value of dielectric loss at high frequency for the sample suggests the enhanced inherent optical quality and few defects in the crystal [42].

The variation of dielectric permittivity at different temperatures are found to be less and having the same values at very high frequencies. This indicates the absence of any phase transitions in the sample.

The dc conductivity of guanidinium 4-aminobenzoate with respect to frequency is shown in Fig. 5. The ac conductivity increases slowly with increasing frequency resulting in a band and on further increase of frequency, the conductivity decreases as shown in the inset of Fig. 5.

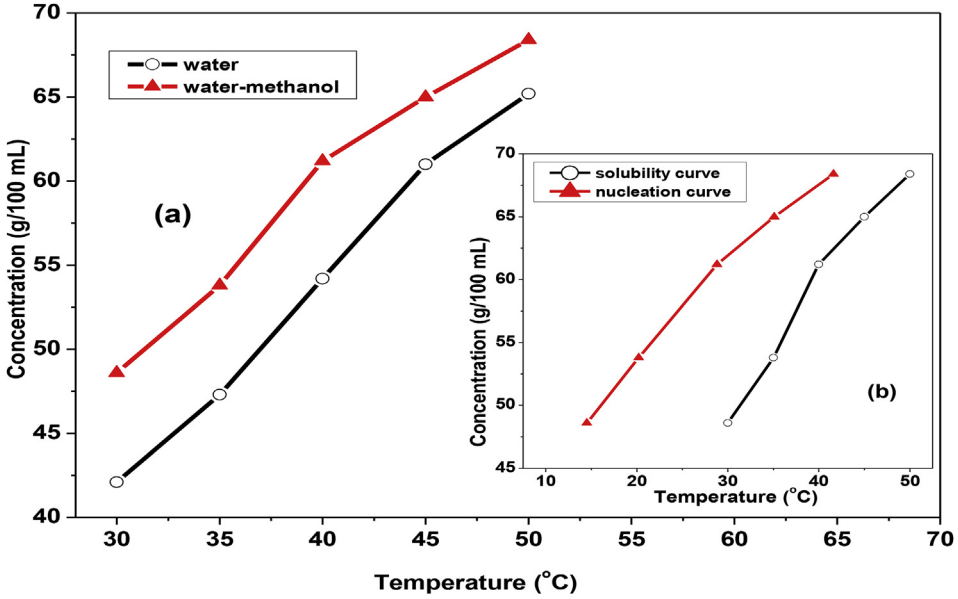

Fig. 2. (a) Solubility of G4AB, (b) The metastable zone width of G4AB single crystal.

This can be explained on the basis of hopping mechanism. With increasing frequency the charge carriers are drift due to the hopping mechanism which results in increasing conductivity [43]. The frequency at which conductivity becomes maximum is termed hopping frequency. Above the hopping frequency the σac conductivity decreases due to charge accumulation and grain boundary interface [44].

The real (M') and imaginary (M") part of dielectric modulus at various temperatures delivers the charge transport mechanism. The electric modulus is obtained from the observed dielectric permittivity studies using the following relations [45].

The electric modulus in terms of complex function is written as;

$$M* = M' + jM''$$

The real and imaginary parts of complex modulus is expressed as,

$$M' = \frac{\varepsilon'}{\varepsilon'^2 + \varepsilon''^2}$$

$$M'' = \frac{\varepsilon''}{\varepsilon'^2 + \varepsilon''^2}$$

Frequency dependent variations of real part M′ of dielectric modulus for G4AB at 35 °C and 100 °C are shown in Fig. 6. Inset shows variation of its imaginary part M" with respect to frequency at 35 °C and 100 °C. M′ shows dispersion tendency at higher frequencies, the value of M' increases with respect to increasing both the frequencies and the temperatures. There are two slope changes observed in the imaginary part of the dielectric spectrum taken at 100 °C. The band found in the high frequency region indicates the dielectric relaxation and that in the low frequency region indicates the conduction region [46]. The band is shifted towards the lower frequency side as the temperature decreases. The nature of dielectric modulus spectrum confirms the hopping mechanism in the electrical conduction of G4AB crystal.

Cole-Cole plot is obtained by plotting real impedance (M') against imaginary impedance (M'')and this complex impedance formalism

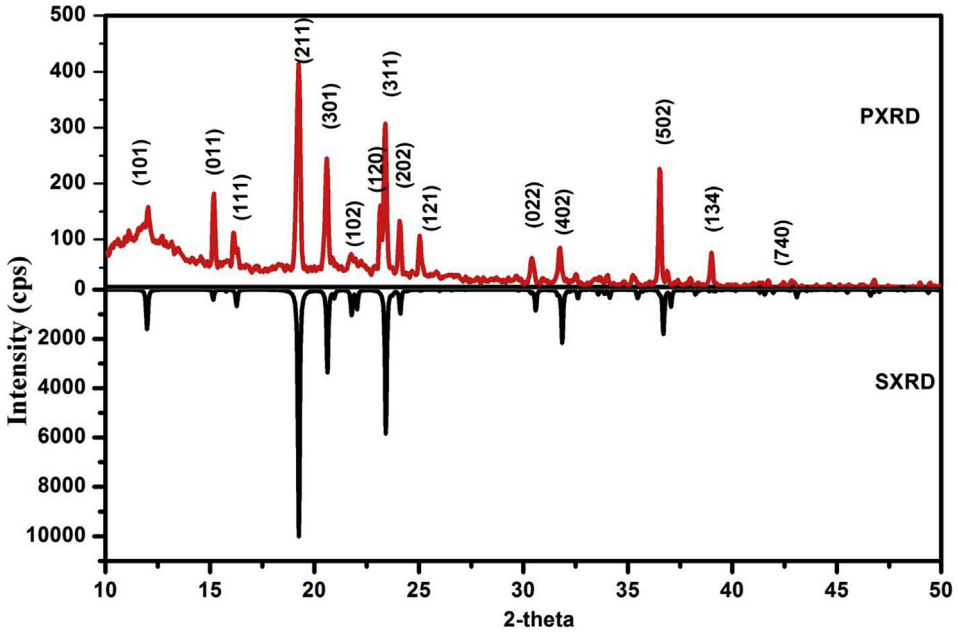

Fig. 3. Experimental PXRD pattern and SXRD pattern of G4AB crystal.

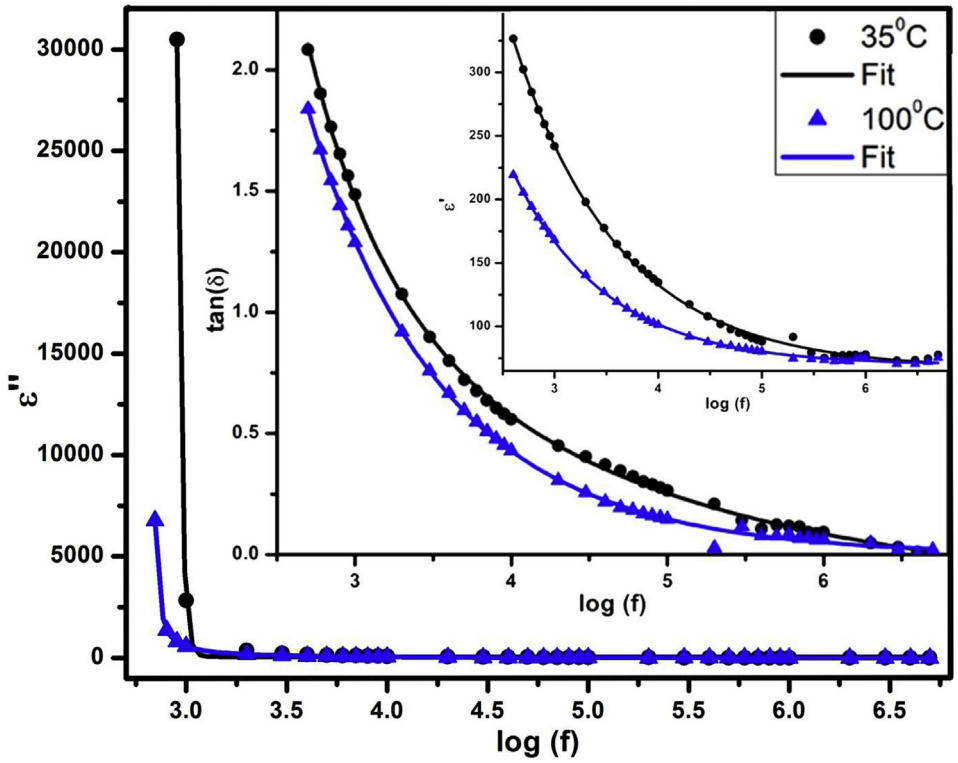

Fig. 4. Frequency-dependent real (ε′) and imaginary (ε″) part of dielectric constant and dielectric loss (tan(δ)) of G4AB at different temperatures.

gives reliable values for the resistance of grains and grain boundaries of crystal. The Cole-Cole plot for G4AB crystal at two different temperatures (35 °C and 100 °C) is shown in Fig. 7. The semi circular appearance confirms the unique role of grain boundaries in the conduction processes [47]. The electric modulus plane plot is used to explain the relaxation phenomenon, if it is sensitive to resistance [48]. In the present cases complex modules have explained the relaxation mechanism satisfactorily than the impedance plot. However the radius of the semicircle varies with temperature. The reason may be that at high temperature, the resistivity of the material is large. The area of semicircles

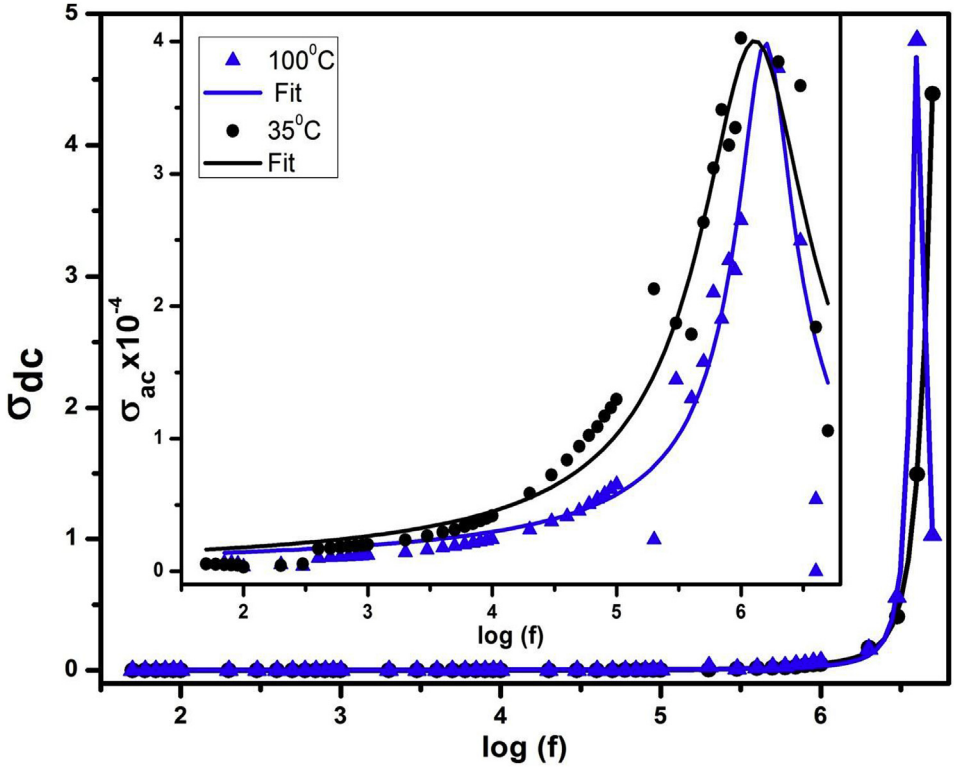

Fig. 5. Frequency dependence of AC and DC conductivities of G4AB crystal at different temperatures.

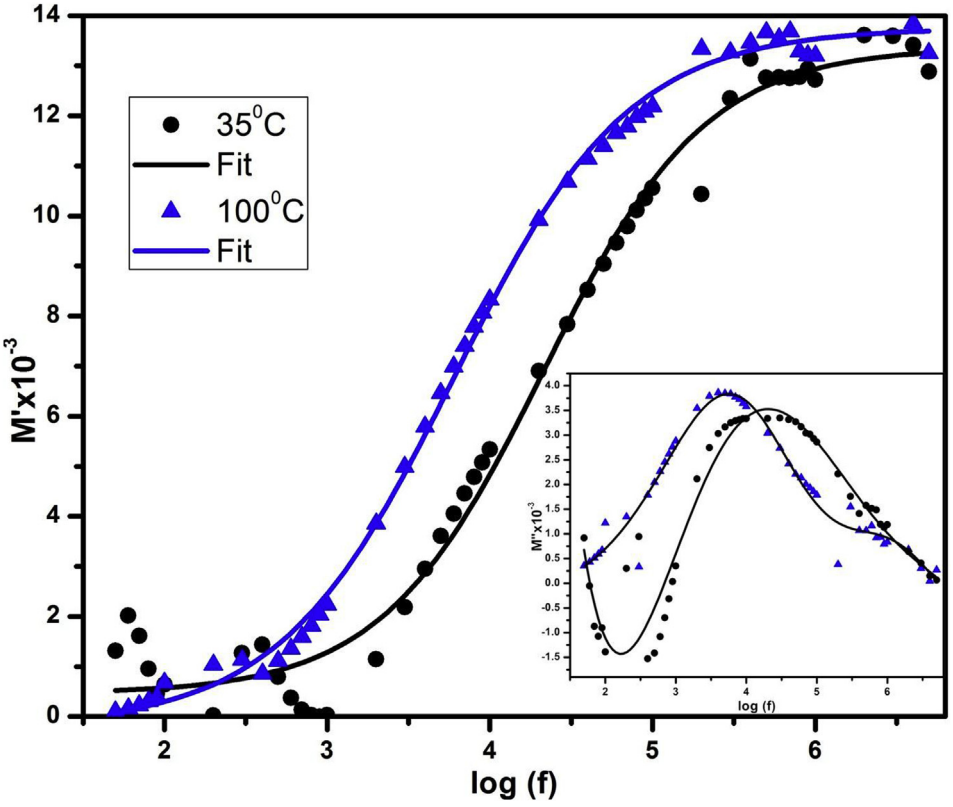

Fig. 6. Frequency dependent variations of real part M′ and imaginary part M" for G4AB with different temperatures.

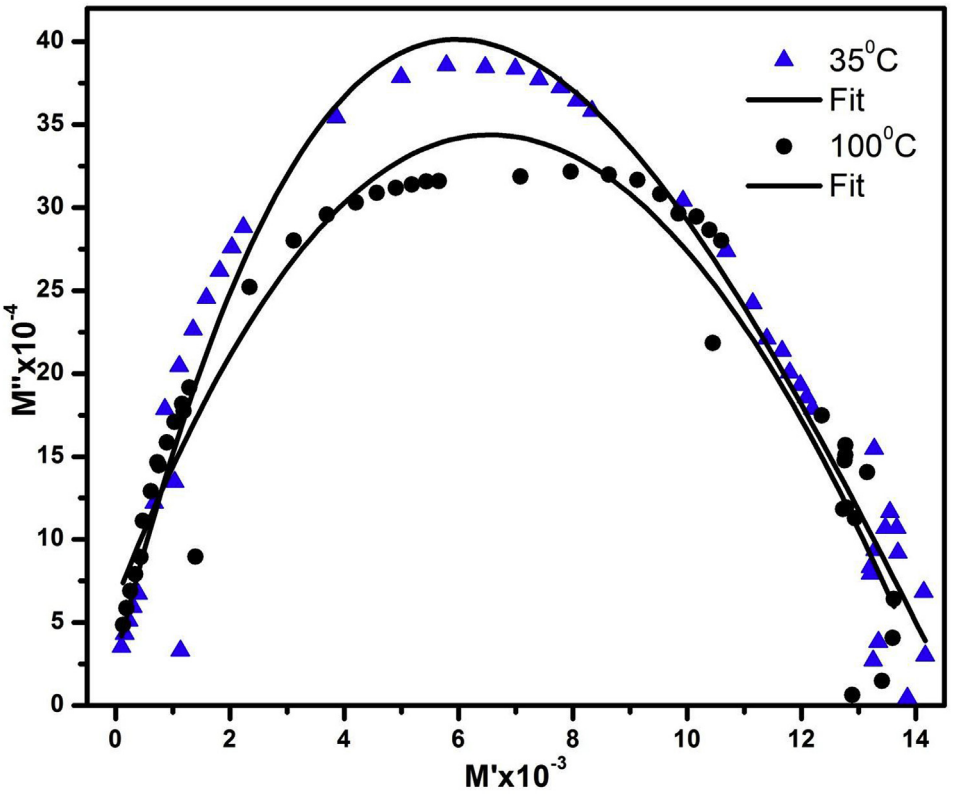

Fig. 7. Cole-Cole plot for G4AB crystal.

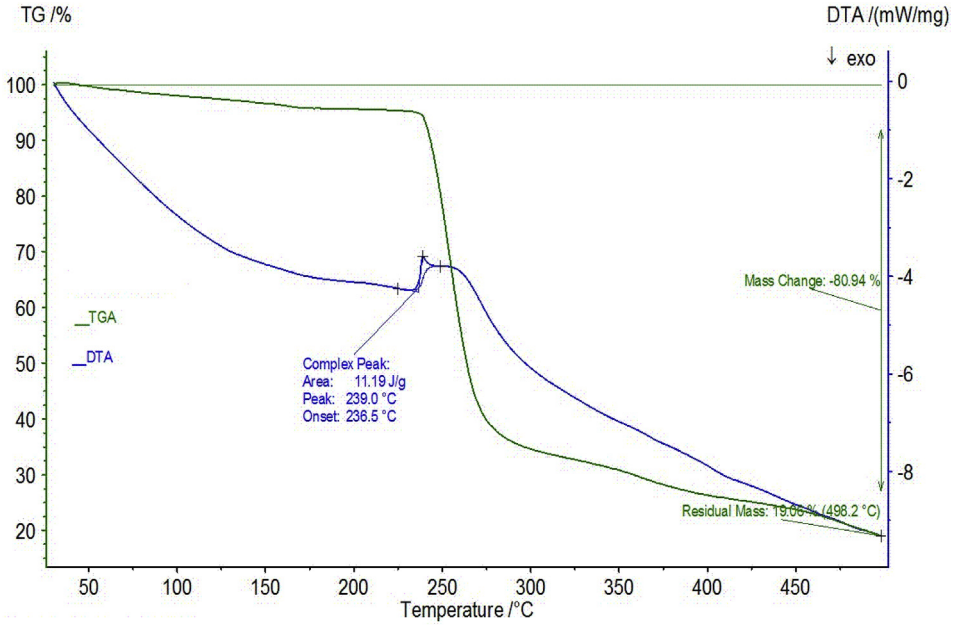

Fig. 8. TG/DTA curves of G4AB.

decrease with the rise in temperature which depicts that the resistance of the crystals decreases with temperature. The two semicircles show only one arc corresponding to the insulating properties of the grain and grain boundary [49]. This indicates that G4AB crystal shows single relaxation time process which corresponds to the bulk dielectric response.

4.3. Thermal studies

The thermal studies were carried out for G4AB crystal using STA 409C instrument analyzer in nitrogen atmosphere at a heating rate of 10 °C/min from 50 °C to 500 °C as shown in Fig. 8. The thermal gravimetric analysis (TGA) shows 80.94% of weight loss. The DTA shows a sharp endothermic band at 239 °C. This endothermic peak matches the weight loss of TGA starting at 236 °C, thereafter no weight loss was observed between 100 °C to 200 °C. This indicates that there is no inclusion of water in the crystal lattice. The final residue weight is 19.06%. Thermogram spectrum reveals that the major weight loss starts at 230 °C and continues up to 270 °C. In the DTA spectrum, an endothermic peak was observed around 239 °C which corresponds to the decomposition temperature of the material. There were no other peaks found below the decomposition temperature, so the crystal is completely free from water of crystallization [50].

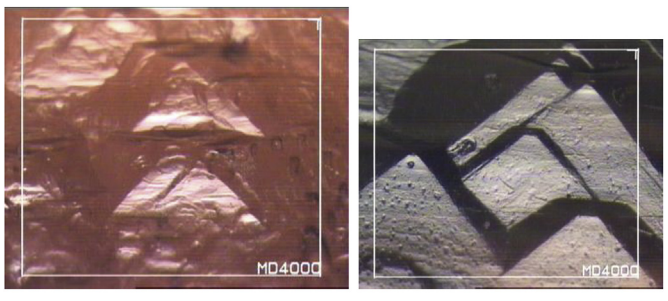

Fig. 9. Etch patterns obtained on G4AB-crystal for different etchants.(a) Water, (b) Methanol.

4.4. Etching studies

The impurities and dislocations that occur during the crystal growth may affect NLO efficiency of the grown crystals. Triangular etch pits were observed when G4AB single crystals was etched with water for 60 s as shown in Fig. 9(a). Similarly, rectangular etch pits were observed when the crystal was etched with methanol for 60 s as shown in Fig. 9(b). The etching behavior of different etchants on G4AB crystals revealed that the presence of dislocation in the crystal by using organic solvents. Fast dissolving etchants like water produce better contrasting dislocation etch pits of all surfaces and hence it is intensive to surface orientation. The observed etch pits indicated that the crystal does not have layered growth with 2D nucleation mechanism and has less dislocations.

4.5. Optimized geometry

The molecular structure of G4AB with the atom numbering is shown in Fig. 10. The selected optimized geometric and the available XRD [51] parameters of the molecule for G4AB are listed in TS1 (supplementary Information). The geometry and planarity of the molecule are strongly perturbed by the orientation of the hydrogen bond donors and acceptors.

The bond distances and bond angles of the computed models of cation and anion molecules model are slightly longer than the experimental ones and the largest discrepancies do not exceed 0.06 Å for bond lengths and 1.135° for bond angles, which is not surprising given that theoretical calculation relates to the isolated molecule whereas the experimental result belongs to the molecule in the solid state where, ascribed to electronic effects of the acceptor –donor groups more than to structural ones and intermolecular Coulombic interactions with the neighbouring molecules are absent. In order to assess the quality of the molecular models, a correlation between the experimental and calculated geometric parameters is shown in Fig. 11. It is found that the molecular model recovered from B3LYP/6-311G(d) in this study is the best representation of the actual molecular structure since the observed value of correlation coefficient by the linear fit is close to one. The intermolecular hydrogen bonds $H_{17}...O_{16}$ and $O_{16}...H_{21}$ have distances of 1.72 Å and 1.73 Å which are much shorter than in the X-ray structure (2.09 Å and 2.10 Å) due to the fact that only a single 4-benzoate anion pair has been considered in the calculation, whereas the three 4-

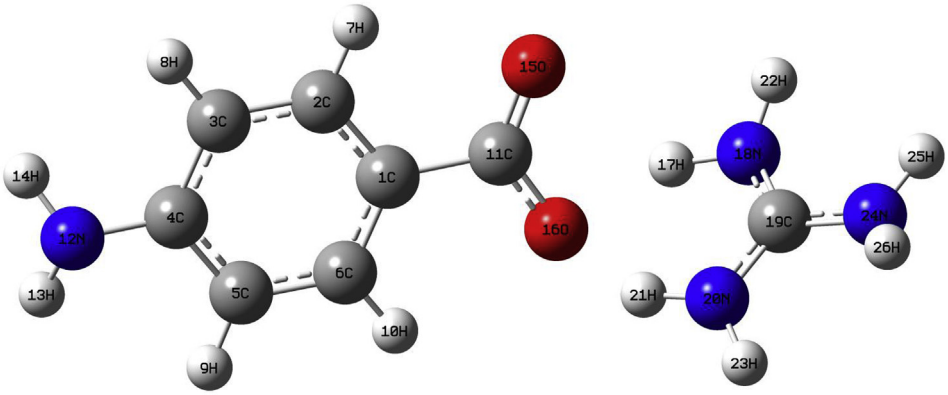

Fig. 10. Optimized molecular structure of G4AB.

benzoate anion molecules are paired with single guanidinium cation molecule in the solid state of G4AB. The mutual geometry and arrangement of cation and anion molecules describe the H_{21}-O_{16}-H_{17} angle in the 73.39° in the DFT, which is in nice agreement with XRD (62.96°).

The optimized molecular structure consists of 4-aminobenzoate anion and guanidinium cation which are structured in a non-planar geometry through the N-H···O hydrogen bonds established between them. The hydrogen bonding geometry given in TS1 categorizes the moderate H-bonding in G4AB. The bond length of C_{11}-O_{16} (1.295 Å) is slightly larger than that of C_{11}-O_{15} (1.239 Å) and is intermediate between a single C-O bond (1.308–1.320 Å) and a double C=O bond (1.214–1.224 Å) [33]. The predicted bond lengths of the two C-O bonds of the carboxylate group indicate its hybrid structure. Due to the simultaneous involvement of the two oxygen atoms in H-bonding, the OCO bond angle of the carboxylate group is expanded to 124.1°. The DFT calculation predicted the two moderate N-H···O bonding in the molecule of G4AB. The NH bonds of guanidinium involved in H-bonding are N_{18}-H_{17} (1.051 Å) and N_{20}-H_{21} (1.040 Å) and they are considerably elongated over the other NH bonds (N_{18}-H_{22}; 1.008 Å, N_{20}-H_{23}; 1.006 Å, N_{24}-H_{25}; 1.006 Å and N_{24}-H_{26}; 1.006 Å) of guanidinium. The CC bond lengths of the benzene ring are found to be in the range 1.388–1.404 Å. The calculated bond length values for the C-N bonds of the guanidinium group are found to be influenced by the H-bonding at the NH sites. The bond lengths predicted for the C_{19}-N_{18}, C_{19}-N_{20} and C_{19}-N_{24} bonds were 1.326 Å, 1.331 Å and 1.359 Å, respectively which are intermediate between those of single- and double-CN bonds, which indicates the increased charge delocalization in the cation moiety. The equal bond length values observed for the C_{19}-N_{20} and C_{19}-N_{24} bonds clearly indicate the formation of intermolecular parallel hydrogen bonding at the two NH_2 groups in the crystalline state. The predicted bond angle values for N_{18}-C_{19}-N_{20}, N_{18}-C_{19}-N_{24} and N_{20}-C_{19}-N_{24} angles of guanidinium were slightly deviated from the corresponding observed values but the sum of these angles around the central carbon (C_{19}) atom was found to be 360° in DFT and XRD data. The two NH bonds of the amino group of 4-aminobenzoate have equal bond lengths and were noticeably elongated over the observed values. According to the X-ray data and calculated geometry, the ring substituted amino group was free from hydrogen bonding interactions at the solid state and the gas phase of G4AB. The observed dihedral angles

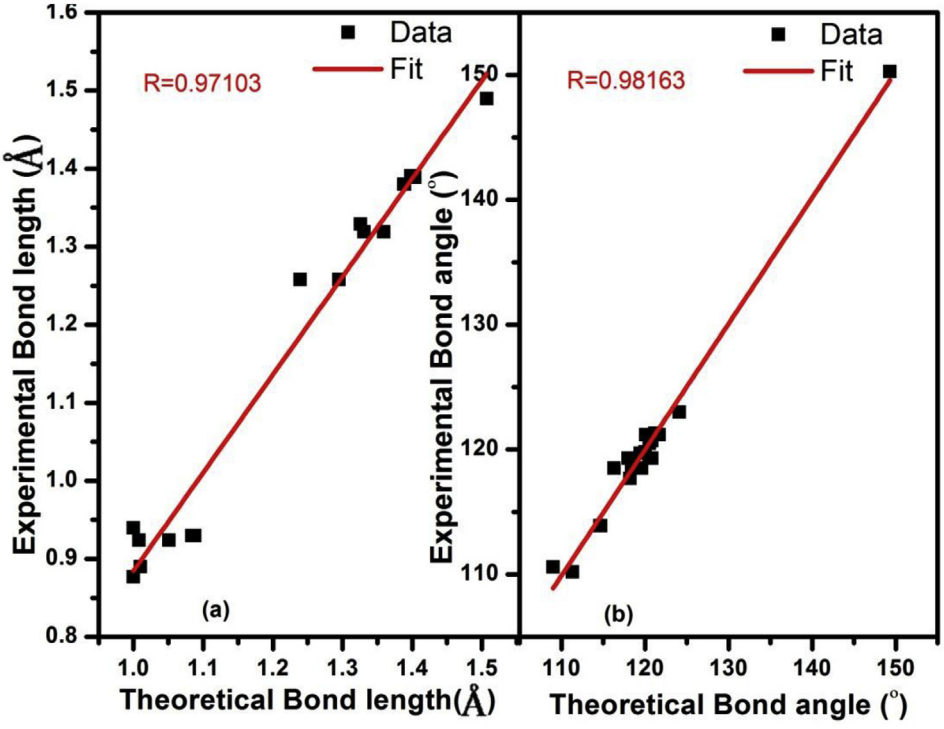

Fig. 11. Correlation graphics of calculated and experimental (a) bond length (b) bond angles of G4AB.

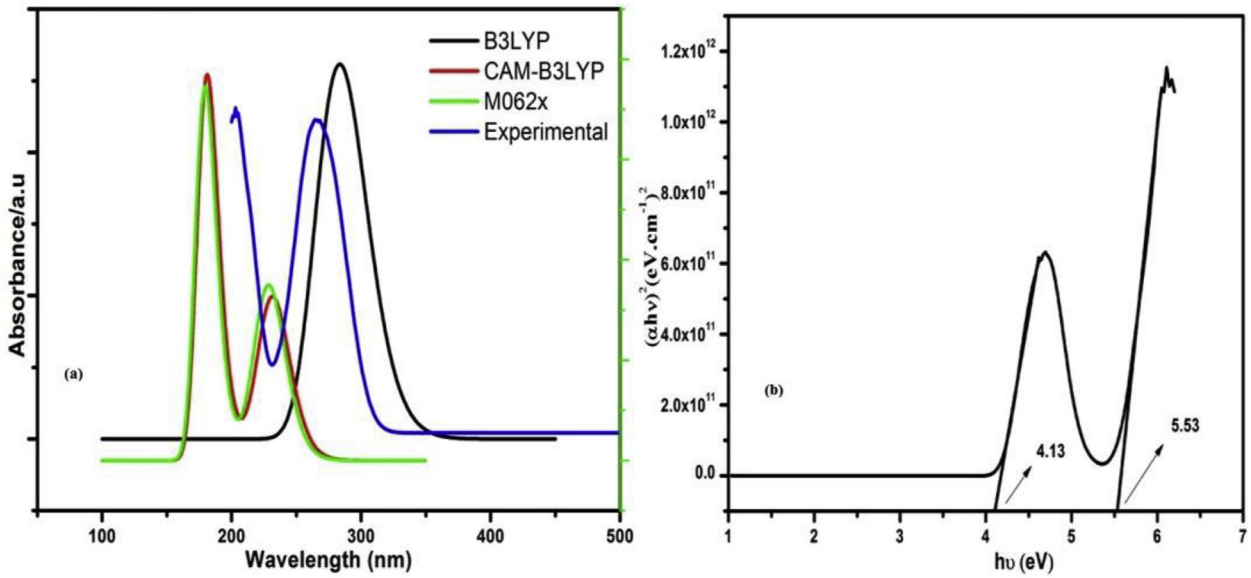

Fig. 12. (a) UV-Vis-NIR experimental and simulated spectra of G4AB in solid phase (b) tauc plot for G4AB.

of C_3-C_4-N_{12}-H_{13} (178.48°), C_3-C_4-N_{12}-H_{14} (1.23°), C_5-C_4-N_{12}-H_{13} (−1.23°) and C_5-C_4-N_{12}-H_{14} (−179.48°) indicate the co-planarity of amino group with the benzene ring within the anionic moiety. But the DFT calculation predicted no such co-planarity for the amino group with the ring for the isolated gas phase molecule. The dihedral angles of $C_{11}O_{16}H_{21}N_{20}$ (−84.4°), $C_{11}O_{16}H_{17}N_{18}$ (115.7°) and $C_{11}O_{15}H_{17}N_{18}$ (−148.2°) clearly indicate the deviation of the plane of the cation moiety from the plane of anion moiety.

4.6. UV-Vis-NIR spectral analysis

The combined experimental and theoretical optical absorption spectrum for G4AB is shown in Fig. 12 (a).

The observed spectrum of the sample in solid phase shows two strong absorption peaks at 204 nm and at 267 nm and the absorption edge is observed around 320 nm. The shorter-wavelength absorption peak at 204 nm is assigned to the π→π* transition due to the carboxylate group and the absorption maximum at 267 nm is due to the presence of amino groups in G4AB. The wide optical transparency in the 320-1100 nm wavelength region indicates the suitability of the crystal in NLO applications and as window in spectral instruments in that region. For a meaningful comparison with the experimental UV/Vis spectrum, the theoretical spectra obtained in the TDDFT calculations were convoluted with Gaussian functions with the appropriate full width at half-maximum (FWHM). The theoretical simulated absorptions spectrum calculated by B3LYP in gas phase of G4AB has an absorption maximum at 280.85 nm with the highest oscillator strength, $f = 0.0057$ which is found to be due to the electron transition from HOMO-1 to the LUMO. The absorption maximum predicted by M062x in gas phase was at 228.28 nm with $f = 0.4179$ and 182.70 nm with f = 0.1750 assigned to the n→π* and π→π* transitions respectively. Whereas in the case of CAM-B3LYP in gas phase of G4AB, the absorption maximum calculated at 231 nm ($f = 0.3874$) and 186.50 nm ($f = 0.1295$) are caused by n→π* and π→π* transitions respectively. The predicted excitation energies, oscillator strengths and absorption maxima for B3LYP, M06-2X and CAM-B3LYP in gas phase of G4AB for the three excitations together with the characteristic molecular orbitals are listed in TS2 (supplementary Information). Among the three TD-DFT methods, the excitation energies calculated with CAM-B3LYP and M06-2X level of theory are reasonably in good agreement with experimental spectrum with larger oscillator strength.

The highest occupied molecular orbital (HOMO) and the lowest unoccupied molecular orbital of G4AB were concentrated entirely over the anionic and cationic moieties, respectively. The HOMO-LUMO plot of G4AB calculated at the B3LYP/6-311G(d) level is shown in Fig. 13.

The calculated energy values of the HOMO, LUMO and HOMO-LUMO gap for the molecule were −5.0194eV, −0.3929eV and 4.6265eV, respectively. The strong electron transitions from the low lying HOMO and LUMO orbitals create an effective charge transfer pathway within the molecule that might cause a highly polarized electronic structure resulting in a strong non-linear optical activity for G4AB. The experimentally obtained band gap energy is shown in Fig. 12(b).

4.6.1. Z-scan studies

Z-scan technique was employed to study the third order nonlinear optical properties such as the magnitude and sign of nonlinear absorption coefficient and nonlinear refractive index of the G4AB crystal. The Nd:YAG laser beam with wavelength 532 nm was focused on the quartz cuvette that containing the sample (G4AB crystal dissolved in methanol solvent) moved through the positive and negative z-directions and corresponding intensity was measured using a photo detector. The nonlinear optical absorption coefficient (β) and nonlinear refractive index (n_2) values were evaluated from the open aperture and closed aperture z-scan, respectively. The open aperture z-scan curve shown in Fig. 14(a) indicates the saturable absorption behaviour at higher intensity near the focus. The nonlinear absorption coefficient (β) can be determined using the relation [52].

$$\beta = \frac{2\sqrt{2}\Delta T}{I_0 L_{eff}} \tag{3}$$

where, $L_{eff} = [1 - \exp(-\alpha L)/\alpha]$ is the effective thickness of the sample, α is the linear absorption coefficient, L is the thickness of cuvette, I_0 is the on-axis irradiance at focus, ΔT is the one valley value at the open aperture Z-scan curve.

The closed aperture z-scan as sown in Fig. 14(b) resembles the negative refraction nonlinearity as a pre-focus peak is followed by a post-focus valley, which is an essential property of materials exhibiting the self-defocusing effect. The nonlinear refractive index (n_2) was calculated from the equation,

$$n_2 = \frac{\Delta\Phi_0}{kI_o L_{eff}}\ cm^2/W$$

where, $k = 2\pi/\lambda$, $L_{eff} = [1 - \exp(-\alpha L)/\alpha]$ is the effective thickness of

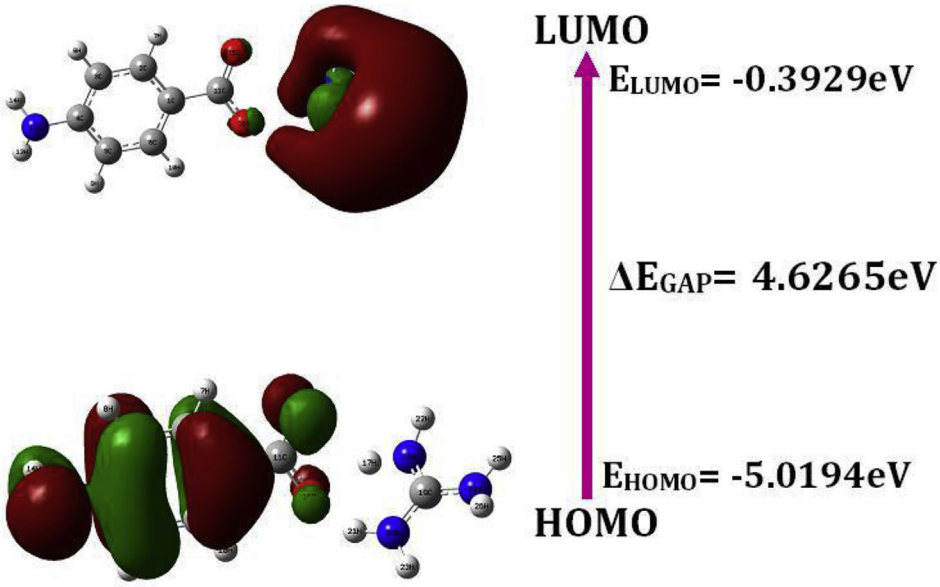

Fig. 13. HOMO-LUMO plot of G4AB.

the sample.

The absolute value of the third-order nonlinear optical susceptibility $\chi^{(3)}$ is

$$|\chi^{(3)}| = [|\mathrm{Re}\chi^{(3)}|^2 + |\mathrm{Im}\chi^{(3)}|^2]^{1/2} \quad (6)$$

The second order hyperpolarizability, γ which defines the nonlinear induced polarization per molecule, [53] is given by,

$$\gamma = \frac{\chi^{(3)}}{NL^4} \quad (7)$$

where N is the number of molecules per unit volume and L is local field correction factor

$$L = \frac{n_0^2 + 2}{3} \quad (8)$$

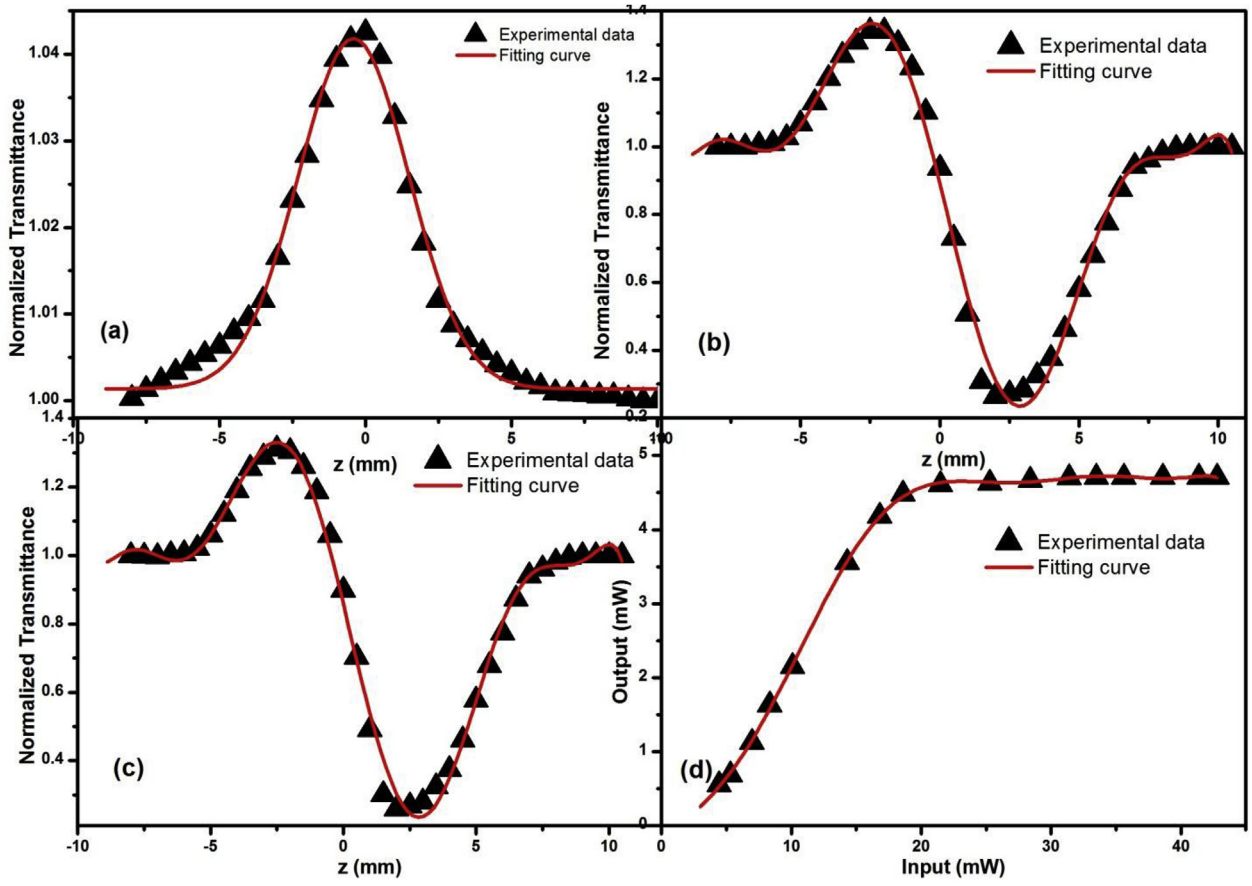

Fig. 14. (a) Open aperture (b) Closed aperture (c) ratio of closed to open aperture z-scan (d) Optical limiting curve for PTM.

Table 1
Nonlinear optical parameters obtained from Z-scan measurement data for G4AB crystal.

Laser beam wavelength (λ)	532 nm
Focal length of Lens(f)	3.5 cm
Power of laser input	50 mW
Optical path distance (Z)	70 cm
Power of the output beam of laser	34.3 mW
Beam radius at the aperture(ω_a)	15 mm
Radius of the laser beam (ω_L)	0.16 mm
Radius of aperture (r_a)	2 mm
Linear refractive index(n_0)	1.04
Linear absorption coefficient (α)	−1.099
Nonlinear refractive index (n_2)	5.34×10^{-8} cm^2/W
Nonlinear absorption coefficient (β)	0.03×10^{-4}cm/W
Real part of third-order susceptibility [Re(χ^3)]	1.46×10^{-6} esu
Imaginary part of third-order susceptibility [Im(χ^3)]	0.19×10^{-6} esu
Third-order nonlinear optical susceptibility (χ^3)	1.47×10^{-6} esu
Second order molecular hyperpolarizability (γ)	3.376×10^{-34} esu

In G4AB, the guanidinium cation carry delocalized electronic cloud and are free of inversion center. The 4-aminobenzoate anion is free from inversion center and engaged to ring aromaticity which was less delocalized compared to guanidinium cation. The closed aperture z-scan shows higher peak-valley difference transmittance indicating the efficiency of the nonlinearity [54]. The calculated results are summarized in Table 1. The optical limiting experiment was carried out by placing the sample at the valley point and the obtained characteristic curve is as shown in Fig. 14(d). The transmitted output intensity was found to vary linearly with input intensity at low intensities but starts to deviate at high intensities reaching a saturation point. i.e, the maximum output intensity shows obvious optical limiting property. The higher values of χ^3 and γ are mainly due to the presence of delocalized π-electronic configuration in the ring structure and effective intermolecular charge transfer interaction between the cations and anions, and that may eventually enhance the third-order optical nonlinearity of G4AB [55].

4.6.2. Molecular NLO response properties

The range-separated functionals like CAM-B3LYP and hybrids with a high percentage of HF exchange as M06-2X were shown to perform better than functionals with low HF exchange, in the determination of field dependent hyperpolarizabilities [56–60]. The hyperpolarizability values of DFT methods M06-2X and CAM-B3LYP are in good agreement for G4AB molecule. The static and the dynamic values of the mean polarizabilities and the anisotropy of the polarizabilities for G4AB and the standard NLO material urea molecule have been calculated with B3LYP, M06-2X and CAM-B3LYP fuctionals with 6-311G(d) basis set and the results are listed in Table 2. The calculated static values of the first-second hyperpolarizabilities are comparable in all the three functionals for the G4AB molecule. The theoretically calculated static-first hyperpolarizability (β_{total}) values reported for guanidium 4-nitrobenzoate was 0.30243×10^{-30} esu [24] and for methyl p-hydroxy benzoate was 2.315×10^{-30} esu [61]. The large value of static β and γ values for G4AB compared to the other organic NLO complexes indicate its superior NLO property. The dynamic first-hyperpolarizability was calculated using a frequency, $\omega = 0.0857$ a.u. for the second harmonic generation $\beta(-2\omega; \omega, \omega)$. The theoretically estimated value of $\beta(-2\omega; \omega, \omega)$ for the G4AB molecule was 92.6521×10^{-30}esu, 35.001×10^{-30}esu and 38.621×10^{-30}esu for the functional B3LYP, M06-2X and CAM-B3LYP which are 45, 42 and 36 times greater than that of urea molecule, respectively. The values of $\gamma(-2\omega; \omega, \omega, 0)$ for the G4AB molecule was 1017.97×10^{-30}esu, 64.229×10^{-30}esu and 74.415×10^{-30}esu for the functional B3LYP, M06-2X and CAM-B3LYP which are 221, 41 and 34 times greater than that of urea molecule, respectively. The calculated values of frequency dependent properties of mean polarizabilities, anisotropy of the polarizability and dynamic first-hyperpolarizability values for G4AB are 1.36, 1.56 and 9.93 times, respectively, greater than those values reported for the organic NLO active guanidinium × maleic acid molecule [62]. The enhancement of first order hyperpolarizability values of G4AB is due to the strong electron transfer interactions from NH sites in the guanidinium cation to oxygen atom in the 4-aminobenzoate through strong π-conjugations in the benzene ring, which is evident from NBO and AIM analysis also.

4.7. NBO analysis

The structure stabilizing natural bond orbital interactions were calculated from the electronic orbitals of G4AB molecule by NBO method and the results of the analysis of selected orbital interactions is presented in ST.3 (supplementary Information).

The NBO analysis predicted two strong n→ π* interactions in the 4-aminobenzoate group due to the lone pairs of the nitrogen and the oxygen atoms which stabilize the molecule through $n_1(N_{12})$→ π*(C_4-C_5) and $n_3(O_{16})$→π*(C_{11}-O_{15}) with second-order perturbation energies of 105.38 kJ/mol and 313.55 kJ/mol, respectively. The combined effect of n→π*, n→σ*, σ→σ* and π→π* NBO donor-acceptor charge delocalizing interactions strengthen the O=C=O bond. Even though both the C_3-C_4 and C_4-C_5 bonds of the benzene ring have identical atomic environment, the σ*(C_3-C_4) and σ*(C_4-C_5) bonds were found to have slight difference in their electron densities and have occupancies of 0.0254*e* and 0.0253*e*, respectively. Also, the C_3-C_4 bond is found to be involved with an n→π* type hyperconjuation in the molecular system and such interactions with the π-antibonding orbital of C_4-C_5 bond, resides it with more π-character resulting in a slight decrement in bond length compared to the C_3-C_4 bond length value. The electron donation from σ(N_{12}-H_{14}) to σ*(C_4-C_5) and from σ(N_{12}-H_{13}) to σ*(C_3-C_4) stabilize the system with delocalization energies of 16.54 kJ/mol and 16.5 kJ/mol, respectively. The NBO analysis for G4AB has identified n→σ* type

Table 2
Comparison of static and field dependent first & second hyperpolarizability, polarizability, and dipole moment for G4AB and urea molecules are calculated with DFT/B3LYP/M062x/CAM-B3LYP/6-311G(d).

		B3LYP(G4AB)	B3LYP (urea)	M062x (G4AB)	M062x (urea)	CAM-B3LYP (G4AB)	CAM-B3LYP (urea)
μtotal (Debye)		8.0340	4.781	8.232	4.879	8.170	4.860
$\alpha(0,0)\times10^{-24}$esu	α_{total}	19.0544	3.964	18.368	3.862	18.415	3.870
	Δα	15.9044	2.552	14.519	2.410	14.669	2.439
$\alpha(-\omega,\omega)\times10^{-24}$esu	α_{total}	20.3737	4.092	19.445	3.971	19.517	3.981
	Δα	18.2217	2.6827	16.264	2.513	16.472	2.547
$\beta(0; 0,0) \times10^{-30}$esu		6.6115	1.31×10^{-7}	4.665	1.31×10^{-7}	4.850	1.25×10^{-7}
$\beta(-\omega; \omega, 0) \times10^{-30}$esu		20.5911	1.183	11.482	0.634	12.197	0.767
$\beta(-2\omega; \omega, \omega) \times10^{-30}$esu		92.6521	2.044	35.001	0.831	38.621	1.069
$\gamma(0; 0,0,0)$ X10^{-36} esu		24.4658	1.563	12.044	0.840	12.998	1.062
$\gamma(-\omega; \omega, 0,0)$ X10^{-36} esu		44.7574	2.0615	17.156	1.003	18.813	1.303
$\gamma(-2\omega; \omega, \omega, 0)$ X10^{-36} esu		1017.979	4.6045	64.229	1.548	74.415	2.185

H-bonding interactions in the molecule with energetic delocalizations of 92.19 kJ/mol for $n_2(O_{16})\rightarrow\sigma^*(H_{17}\text{-}N_{18})$ and 32.11 kJ/mol for $n_1(O_{16})\rightarrow\sigma^*(H_{20}\text{-}N_{21})$. The hyperconjugative interactions due to the lone pairs of oxygen atoms with the $H_{17}\text{-}N_{18}$ dominates energetically than those with the σ*-orbital of $H_{20}\text{-}N_{21}$ bond. The $n(O)\rightarrow\sigma^*(H\text{-}N)$ interactions accumulate an enormous electron occupancy of 0.0796*e* on the $\sigma^*(H_{17}\text{-}N_{18})$ and an occupancy of 0.0551*e* on the $\sigma^*(H_{20}\text{-}N_{21})$. As a result of these interactions, the $H_{17}\text{-}N_{18}$ bond length is slightly elongated as compared to that of the $H_{20}\text{-}N_{21}$ bond. In G4AB, the simultaneous involvement of two of the cationic nitrogen atoms in H-bonding hindered the efficient spread of π-conjugative resonance charge transfer in guanidinium. However, the charge transfer by H-bonding as well as the hyperconjugative resonance interactions gives a highly delocalized structure to the guanidinium cation.

4.8. Electron-hole transport properties

The electron-hole transfer rate depends on structural factors such as degree of conjugation between the donor - acceptor sites in the organic molecules. The vertical and adiabatic electron affinities (VEA & AEA), vertical and adiabatic ionization potential (VIP & AIP) and electron – hole reorganization energies ($\lambda_{electron}$ & λ_{hole}) are important parameters for the evaluation of the transport rates of holes and electrons. The electron-hole reorganization energies and vertical and adiabatic electron affinities can be defined as follows [63]:

$$\lambda_{electron} = (E_0^- - E_-^-) + (E_-^0 - E_0^0)$$

$$AEA = E_-^- - E_0^0$$

$$VEA = AEA + (E_0^- - E_-^-)$$

where E_0^0 and E_-^- are the optimized energy of the neutral and anionic states, and E_0^- and E_-^0 are the energy of the neutral molecule at the anionic state and the energy of the anionic molecule at the neutral state.

$$\lambda_{hole} = (E_0^+ - E_+^+) + (E_+^0 - E_0^0)$$

$$AIP = E_+^+ - E_0^0$$

$$VIP = AIP + (E_0^+ - E_+^+)$$

where E_0^0 and E_+^+ are the optimized energy of the neutral and cationic states, and E_0^+ and E_+^0 are the energy of the neutral molecule at the cationic state and the energy of the anionic molecule at the neutral state.

The basic requirements for charge transfer materials are that they possessing high electron mobility and low reorganization energy [72]. The calculated values as shown in Table 3 reveal a smaller value of λ_{hole} compared with that of $\lambda_{electron}$.

4.9. AIM analysis

The atoms in molecules theory (AIM), is a very useful tool in analyzing the hydrogen bond. The formation of hydrogen bonds is associated to the presence of a bond critical point (BCP) between the hydrogen atom of donor group and acceptor atom which are linked by the associated bond path. Topological and energy parameters for the interacting atoms are listed in Table 4. According to Rozas et al. [52] the interactions may be classified as follows: (i) for strong H-bonds ($\nabla^2\rho(r) < 0$, $H < 0$) and covalent in nature, (ii) for medium ($\nabla^2\rho(r) > 0$, $H < 0$) and partially covalent in nature and (iii) for weak H-bonds ($\nabla^2\rho(r) > 0$, $H > 0$) and electrostatic in nature. The small electron density and positive values of the Laplacian between $H_{17}\ldots O_{16}$ and $O_{16}\ldots H_{21}$ in the molecular complexes indicate a closed shell interaction ($\nabla^2\rho(r) > 0$). Moreover, the Laplacian between other parameters are always negative ($\nabla^2\rho(r) < 0$), which implies that a shared interaction is present in it. The measured $H_{17}\ldots O_{16}$ and $H_{21}\ldots O_{16}$ contacts are in the range 1.723 and 1.732 Å associated with the maximum of electron density at H...O BCP-ρ(r) 0.297 and 0.348 a.u respectively. These results also support that there is a stronger interaction than that of a conventional hydrogen bond as shown in Fig. 15.

Table 3
Ionization potentials (VIP & AIP), electron affinities (VEA & AEA), reorganization energies calculated at B3LYP/6-311G(d) level.

VEA (a.u)	AEA (a.u)	AIP (a.u)	VIP (a.u)	$\lambda_{electron}$ (a.u)	λ_{hole} (a.u)
0.04444	0.00187	0.2343	0.4708	0.1178	0.0378

Table 4
Topological parameters for bonds of interacting atoms: electron density (ρ_r), Laplacian of electron density ($\nabla^2\rho_r$), electron kinetic energy density (G), electron potential energy density (V), total electron energy density (H), at bond critical point (BCP).

Bond	ρ(r)	$\nabla^2\rho(r)$	V	G	H	ε	E
$C_{11}\text{-}C_1$	0.307	−0.853	−0.410	0.098	−0.312	0.189	128.63
$C_2\text{-}C_1$	0.310	−0.867	−0.423	0.103	−0.32	0.218	132.4
$C_2\text{-}C_3$	0.021	0.158	−0.024	0.031	0.007	0.222	7.50
$C_3\text{-}C_4$	0.307	−0.851	−0.410	0.098	−0.312	0.192	128.63
$C_1\text{-}C_6$	0.304	−0.837	−0.405	0.097	−0.308	0.224	126.75
$C_4\text{-}C_5$	0.295	−0.859	−0.533	0.159	−0.374	0.065	166.91
$C_4\text{-}N_{12}$	0.339	−1.541	−0.504	0.059	−0.445	0.055	158.13
$N_{12}\text{-}H_{13}$	0.310	−0.863	−0.421	0.102	−0.319	0.218	131.77
$C_6\text{-}C_5$	0.283	−0.984	−0.318	0.036	−0.282	0.011	99.77
$H_7\text{-}C_2$	0.276	−0.931	−0.316	0.041	−0.292	0.029	99.14
$H_8\text{-}C_3$	0.276	−0.929	−0.316	0.041	−0.275	0.029	99.14
$C_5\text{-}H_9$	0.283	−0.981	−0.319	0.036	−0.283	0.013	99.77
$C_6\text{-}H_{10}$	0.339	−1.54	−0.504	0.050	−0.454	0.055	158.13
$H_{14}\text{-}N_{12}$	0.389	−0.363	−1.19	0.550	−0.64	0.063	373.36
$O_{15}\text{-}C_{11}$	0.342	−0.538	−0.922	0.394	−0.528	0.006	289.27
$C_{11}\text{-}O_{16}$	0.047	0.123	−0.042	0.036	−0.006	0.004	13.17
$H_{17}\ldots O_{16}$	0.297	−1.56	−0.483	0.046	−0.004	0.032	151.22
$N_{18}\text{-}H_{17}$	0.015	0.085	−0.013	0.017	0.004	0.192	3.765
$N_{18}\text{-}C_{19}$	0.042	0.133	−0.038	0.036	−0.002	0.065	11.92
$H_{21}\ldots O_{16}$	0.348	−1.11	−0.690	0.020	−0.67	0.189	216.48
$C_{19}\text{-}N_{20}$	0.340	−1.63	−0.543	0.054	−0.489	0.048	170.05
$N_{20}\text{-}H_{23}$	0.306	−1.62	−0.498	0.045	−0.453	0.039	156.24
$N_{20}\text{-}H_{21}$	0.338	−1.62	−0.623	0.184	−0.439	0.04	195.15
$H_{22}\text{-}N_{18}$	0.325	−1.01	−0.505	0.048	−0.457	0.142	158.13
$N_{24}\text{-}C_{19}$	0.340	−1.65	−0.520	0.053	−0.467	0.056	163.15
$H_{25}\text{-}N_{24}$	0.339	−1.64	−0.519	0.054	−0.465	0.057	162.52

4.10. Vibrational spectral analysis

The combined experimental and simulated vibrational spectra of G4AB are shown in Figs. 16 and 17. The calculated values of wavenumbers, IR and Raman intensities, and vibrational assignments for each mode of vibrations along with the fundamental wavenumbers are presented in Table 5.

4.10.1. Vibrations of guanidinium cation

The stretching vibrations of NH_2 group is usually observed in the range 3500–3300 cm^{-1} [64–66]. The PED gives the contributions from the asymmetric and symmetric stretching vibrations of the non-hydrogen bonded NH_2 group at 3559 cm^{-1} and 3452 cm^{-1}, respectively, as well as the non-hydrogen bonded NH stretching modes at 3518 cm^{-1} and at 3487 cm^{-1}. But due to the involvement in H-bonding interactions with the carboxylate group of 4-aminobenzoate, the NH stretching modes of guanidinium are red shifted to 3008 cm^{-1} and 2820 cm^{-1} in the IR as well as to 2953 cm^{-1} and 2752 cm^{-1} in the Raman spectra. The DFT calculations also substantiate the presence of H-bonding in the molecule and predicted NH···O stretching mode at 2953 cm^{-1} and 2752 cm^{-1} with the PED contributions of 90% and 91% for the modes. For the normal N-H···O red-shifted hydrogen bonds, electron transfers from the lone pair electron of electron donator to the σ*(N-H) of the

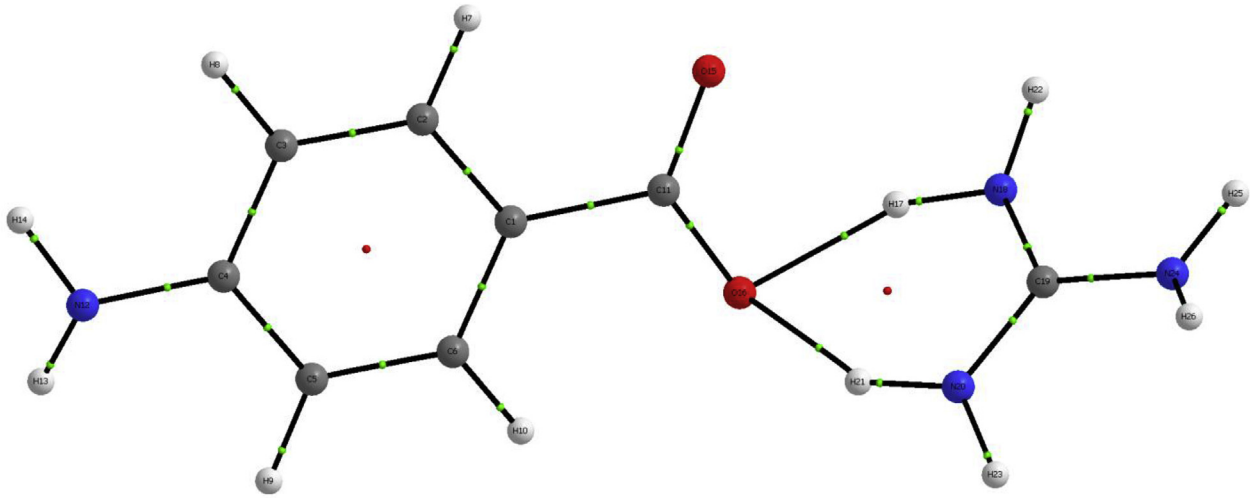

Fig. 15. Molecular graph of the compound at B3LYP/6-311G(d) using AIM program.

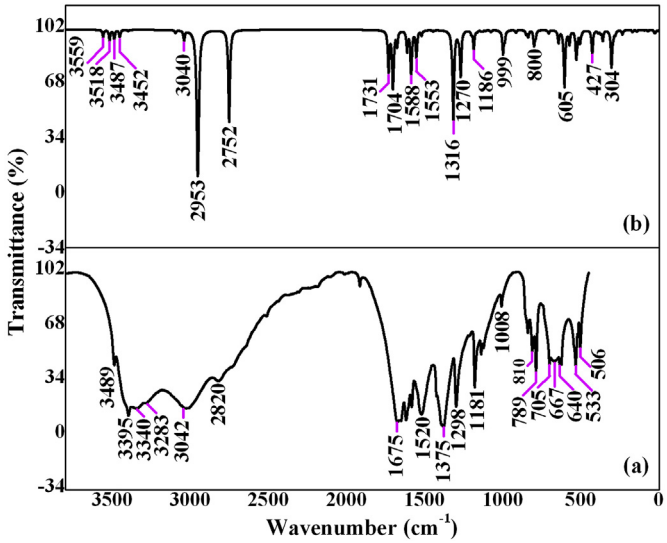

Fig. 16. (a) Experimental, (b) Simulated FT-IR spectra of G4AB.

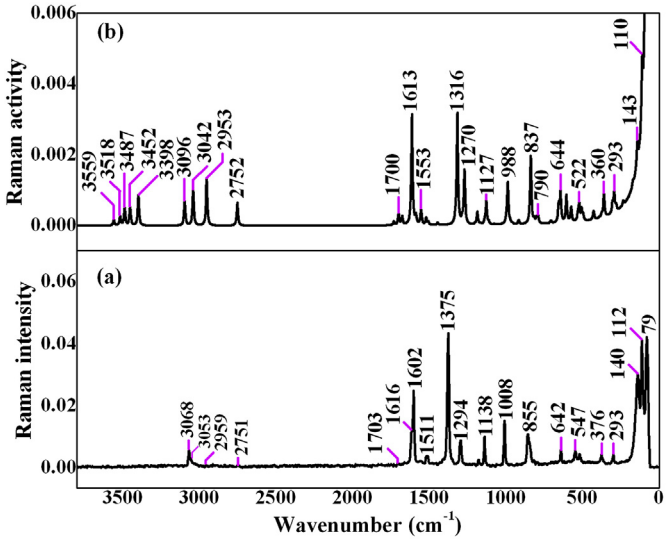

Fig. 17. (a) Experimental, (b) Simulated FT-Raman spectra of G4AB.

electron acceptor, which elongates the N-H bond and leads to a red shift [67]. The scissoring vibrations of amino group are expected in the region 1700-1600 cm^{-1} [68]. The scissoring modes of the NH_2 groups of guanidinium are identified from the strong band at 1675 cm^{-1} in the IR and the weak band at 1511 cm^{-1} in the Raman spectra. The PED reveals the contribution of these modes in the region 1731-1506 cm^{-1} for G4AB. The rocking deformation vibrations of the amino group are usually observed in the region 1150-1100 cm^{-1}. The rocking modes of unperturbed NH_2 group of guanidinium is predicted with 67% of PED at 1111 cm^{-1} and the fundamental bands were absent for the mode. The weak band observed in the IR spectrum at 1212 cm^{-1} can be assigned to the rocking modes of the H-bonded amino group of guanidinium. The PED of these modes are found to be 16% at 1201 cm^{-1} and 20% at 1164 cm^{-1}.

The CN stretching modes of guanidine are usually observed around 1689-1500 cm^{-1} [69,70]. The CN asymmetric and symmetric bond stretching modes of a guanidinium derivative are generally observed at 1649 cm^{-1} and 976 cm^{-1}, respectively [71]. A strong absorption band observed in the IR spectra at 1583 cm^{-1} and corresponding Raman band at 1602 cm^{-1}, the weak Raman band at 1511 cm^{-1}, the weak IR bands at 1212 cm^{-1} and 1008 cm^{-1} and the medium strong IR band at 625 cm^{-1} are also attributed to the stretching vibrations of CN bonds of guanidinium. The down shifting of this mode signifies the charge delocalization in the $C_{19}N_{18,20,24}$ bonds due to the simultaneous involvement of H-bonding at the $N_{20}H_{21}$ and $N_{18}H_{17}$ sites which results in the shortening of $C_{19}N_{18,20}$ bond lengths and weakening of $C_{19}N_{24}$ bond length.

The in-plane CNH bending vibrations are expected in the region 1570-1515 cm^{-1}. The in-plane CNH bending modes of similar guanidinium derivatives are in the wavenumber region 1686-1600 cm^{-1} [63]. The in-plane CNH bending modes of G4AB are observed as strong bands in the IR spectrum at 1675 cm^{-1} and 1583 cm^{-1} whereas in the Raman spectrum, these modes are observed as a medium strong band at 1602 cm^{-1} and a weak band at 1553 cm^{-1}.

4.10.2. *Vibrations of 4-aminobenzoate anion*

The normal vibrations of the para-disubstituted benzene ring were assigned using Wilson's numbering scheme [73]. The bands related to the 2, 20b, 20a and 7b modes of the CH stretching vibrations of G4AB were identified from the Raman spectrum at 3068 cm^{-1}, 3053 cm^{-1}, 3040 cm^{-1} and 3029 cm^{-1}, respectively. The corresponding IR bands were observed as broad band at 3042 cm^{-1}. The DFT calculations predicted the PED contributions of 99% for each CH stretching modes at 3096 cm^{-1}, 3094 cm^{-1}, 3042 cm^{-1} and 3040 cm^{-1} respectively. The CH in-plane and out-of-plane bending modes of *p*-disubstituted benzene

Table 5
Observed FT-IR, FT-Raman and scaled wavenumbers (in cm^{-1}), IR intensities, Raman activities and vibrational assignments of G4AB.

Scaled[a]	FT-IR	FT-Raman	Mode	IR intensity[b] (KM/Mole)	Raman Intensity[c] (Å^4/AMU)	Assignment of each mode with PED in %
3559				1.87	21.7	$\upsilon_{as}(H_{25}N_{24}H_{26})$ (100)
3518				2.93	34.9	$\upsilon(N_{20}H_{23})$ (100)
3488	3489 ms			0.19	30.5	$\upsilon_{as}(H_{13}N_{12}H_{14})$ (100)
3487				2.31	31.3	$\upsilon(N_{18}H_{22})$ (99)
3452				1.98	62.6	$\upsilon_{s}(H_{25}N_{24}H_{26})$ (99)
3398	3395 s			0.27	100	$\upsilon_{s}(H_{13}N_{12}H_{14})$ (100)
3096		3068 w	2	0.09	48.7	υ(CH) (99)
3094		3053 w	20b	0.63	10.9	υ(CH) (99)
3042	3042 s	3040 w	20a	1.16	46.4	υ(CH) (99)
3040	3030 s	3029 w	7b	1.53	36.7	υ(CH) (99)
2953	3008 s	2953 vw		100	99	υ(NH···O) (90)
2752	2820 ms	2752 vw		36.3	40.4	υ(NH···O) (91)
1731		1730 vw		12.7	2.25	β(CNH) (40), $\chi(NH_2)_g$ (16), υ_{as}(OCO) (11), $\chi(NH_2)_{ug}$ (9), $\upsilon(C_{19}N)$ (6)
1704		1703 vw		16.9	0.66	$\upsilon(C_{19}N)$ (36), $\chi(NH_2)_{ug}$ (21), β(CNH) (19), $\chi(NH_2)_g$ (8)
1700		1693 vw		4.08	6.42	$\chi(NH_2)_{ring}$ (95)
1677	1675 s	1663 vw		4.21	4.97	$\chi(NH_2)_{ug}$ (41), $\upsilon(C_{19}N)$ (16), $\chi(NH_2)_g$ (14), β(CNH) (11), β(NH···O) (6)
1613	1618 s	1616 w	8a	5.9	60.6	$\upsilon(CC)_{ring}$ (62), β(CCH) (22), β(CCC) (9)
1588	1583 s	1602 ms		7.87	3	$\upsilon(CC)_{ring}$ (28), $\upsilon(C_{19}N)$ (20), β(CNH) (17), $\upsilon(C_{11}O_{15})$ (10), $\chi(NH_2)_{ug}$ (5)
1585				6.46	1.38	$\upsilon(C_{19}N)$ (32), $\upsilon(CC)_{ring}$ (25), $\chi(NH_2)_g$ (16)
1553		1553 w		7.8	7.81	$\upsilon(C_{11}O_{15})$ (53), $\upsilon(CC)_{ring}$ (16), β(CNH) (7), $\chi(NH_2)_g$ (6)
1520	1520 s		19a	1.35	3.35	β(CCH) (54), $\upsilon(CC)_{ring}$ (37), $\upsilon(C_4N)$ (7)
1506		1511 w		0.08	1.33	$\chi(NH_2)_g$ (46), $\upsilon(C_{19}N)$ (16), β(NH···O) (13), $\rho(NH_2)_{ug}$ (5)
1446	1428 s	1454 vw	8b	0.38	1.13	β(CCH) (42), $\upsilon(CC)_{ring}$ (38), $\rho(NH_2)_{ring}$ (9), β(CCN) (5)
1331	1395 s	1410 vw	14	0.62	1.11	β(CCH) (66), $\upsilon(CC)_{ring}$ (20), $\rho(NH_2)_{ring}$ (8)
1316	1375 vs	1375 vs		34.9	42.8	$\upsilon(C_{11}O_{16})$ (38), $\upsilon(CC)_{ring}$ (28), χ(OCO) (12), β(CCH) (6)
1285	1298 s	1294 w		1.44	1.99	$\upsilon(CC)_{ring}$ (72), β(CCH) (11), $\rho(NH_2)_{ring}$ (6)
1270				14.3	19.4	$\upsilon(C_4N)$ (47), $\upsilon(CC)_{ring}$ (20), β(CCH) (10), β(CCC)$_{ring}$ (10), $\upsilon(C_{11}O_{16})$ (7)
1201	1212 w	1210 vw		0.89	0.25	β(NH···O) (24), $\upsilon(C_{19}N)$ (22), $\rho(NH_2)_g$ (16), δ(CNH) (14), τ(O···HNC) (9), τ ($N_{20}C_{19}$) (5)
1186	1181 s	1178 vw		5.54	4.13	β(CCH) (67), $\upsilon(CC)_{ring}$ (24)
1164				0.39	0.3	β(NH···O) (28), $\upsilon(C_{19}N)$ (24), $\rho(NH_2)_g$ (20), δ(CNH) (15)
1137	1138 ms	1138 ms		0.35	0.99	$\upsilon(C_1C_{11})$ (39), β(CCH) (38), $\rho(NH_2)_{ring}$ (21)
1127	1121 ms			0.28	6.91	$\upsilon(C_1C_{11})$ (46), υ_{s}(OCO) (16), β(CCH) (15), β(CCC)$_{ring}$ (13)
1111				0.2	0.63	$\rho(NH_2)_{ug}$ (67), δ(CNH) (9), $\upsilon(C_{19}N)$ (8), $\rho(NH_2)_g$ (5)
1076		1076 vw		0.53	0.17	$\upsilon(CC)_{ring}$ (40), $\rho(NH_2)_{ring}$ (33), β(CCH) (20)
1023		1028 vw		0.15	0.12	β(CCC)$_{ring}$ (51), $\upsilon(CC)_{ring}$ (36), β(CCH) (13)
999	1008 w	1008 ms		6.75	0.91	Γ(O···HNC) (67), $\upsilon(C_{19}N)$ (8), $\omega(NH_2)$ (7), $\tau(N_{18}C_{19})$ (6)
988				2.43	10.2	Γ(O···HNC) (45), $\upsilon(C_{19}N)$ (37), $\tau(N_{18}C_{19})$ (6)
973		970 vw	5	0.16	0.57	ω(CH) (78), p(CCC) (13)
959		958 vw	17a	0.03	0.22	ω(CH) (89)
917		928 vw		0.68	0.85	$\tau(C_{19}N_{18}H_{17}\cdots O_{16})$ (33), $\tau(C_{19}N_{20}H_{21}\cdots O_{16})$ (32), β(CO···H) (11), $\omega(C_{11}O_{16}H_{17}H_{21})$ (8), $\omega(NH_2)_g$ (6), Γ(O···HNC) (6)
851		855 ms	10b	1.11	0.18	ω(CH) (48), ω(OCO) (14), $\omega(C_4N_{12}CC)$ (9), $\omega(C_{11}C_1CC)$ (8), τ(CCCC) (8)
837	839 ms			1.92	13	$\upsilon(CC)_{ring}$ (41), χ(OCO) (11), β(CCC) (10), $\upsilon(C_4N)$ (7), τ(O···HNC) (5)
814	810 ms	815 vw	10a	0	0.76	ω(CH) (98)
800				4.29	0.88	χ(OCO) (22), p(CCC) (12), ω(OCO) (10), $\upsilon(C_1C_{11})$ (9), $\omega(C_4N_{12}CC)$ (6), δ(CCC)$_{ring}$ (6)
790	789 ms		11	1.55	1.24	p(CCC) (23), ω(CH) (18), ω(OCO) (16), $\omega(C_4N_{12}CC)$ (11), χ(OCO) (7)
708			4	0.41	0.11	p(CCC) (51), $\omega(N_{24}C_{19}N_{18}N_{20})$ (12), ω(CH) (11), $\omega(C_4N_{12}CC)$ (11), ω(OCO) (6)
706	705 ms		4	0.49	0.3	$\omega(N_{24}C_{19}N_{18}N_{20})$ (58), p(CCC) (15), $\tau(C_{19}N_{20})$ (9)
656	667 ms			0.04	2.27	δ(CCC) (60), β(CCC) (23), $\upsilon(C_1C_{11})$ (9)
644	640 ms	642 w		3.44	3.98	$\omega(NH_2)_{ring}$ (42), β(CCC) (14), $\upsilon(C_1C_{11})$ (10), χ(OCO) (10), δ(CCC) (6)
605	625 ms			18.7	3.26	$\omega(NH_2)_{ring}$ (45), $\upsilon(C_{19}N)$ (23), χ(OCO) (7)
574				3.76	1.63	β(NH···O) (43), υ(O···H) (21), $\omega(NH_2)_g$ (11), $\tau(NC_{19})$ (5)
530	533 ms	547 w		7.96	0.64	$\omega(NH_2)_g$ (28), ρ(OCO) (24), $\beta(C_{11}C_1C)$ (5)
522		520 w		1.76	1.58	β(NH···O) (16), $\omega(NH_2)_g$ (15), ρ(OCO) (13), δ(NCN) (10), $\tau(N_{20}C_{19})$ (5)
506	506 ms		16b	3.2	1.03	$\omega(C_4N_{12}CC)$ (26), τ_{out}(CCCC) (25), $\omega(C_{11}C_1CC)$ (14), τ_{in}(CCCC) (8), ω(CH) (6), p(CCC) (5)
496		498 vw		0.61	0.51	δ(NCN) (46), $\omega(NH_2)_g$ (14), δ(NH···O) (11), υ(O···H) (8)
428		436 vw	16a	4.32	0.37	τ_{in}(CCCC) (25), $\omega(NH_2)_g$ (21), $\tau(C_{19}N_{24})$ (13), ω(CH) (8), δ(NCN) (8), τ_{out}(CCCC) (7)
427			16a	2.55	0.26	τ_{in}(CCCC) (39), $\omega(NH_2)_g$ (13), ω(CH) (12), τ_{out}(CCCC) (11), $\tau(C_{19}N_{24})$ (8)
390				0.68	0.08	δ(CCN) (38), δ(CCC) (13), β(NH···O) (10), υ(O···H) (9), $\upsilon(C_1C_{11})$ (8)
374		376 w		0.83	0.19	δ(CCN) (25), β(CCC) (17), $\upsilon(C_1C_{11})$ (13), $\omega(NH_2)_g$ (11), $\tau(C_{19}N_{24})$ (9)
360				2.83	1.29	$\omega(NH_2)_g$ (41), $\tau(C_{19}N_{24})$ (24), $\tau(N_{18}C_{19})$ (11)
304				11.1	0.41	$\omega(NH_2)_{ug}$ (57), $\upsilon(C_{19}N)$ (12), $\omega(NH_2)_g$ (9)
293		293 w		1.13	0.78	$\omega(C_{11}C_1CC)$ (26), p(CCC) (12), τ_{out}(CCCC) (12), $\omega(NH_2)_{ug}$ (9), ω(CH) (7), $\omega(NH_2)$ (5)
280		281 vw		0.94	0.18	$\Gamma(NH_2)$ (91)
235		231 vw		1.21	0.13	υ(O···H) (26), β(NH···O) (22), $\delta(C_{11}C_1C)$ (17), $\omega(C_{11}O_{16}H_{17}H_{21})$ (9), $\upsilon(CC)_{ring}$ (5)
170				0.55	0.08	$\delta(C_{11}C_1C)$ (24), δ(CO···H) (23), υ(O···H) (12), ρ(OCO) (8), β(NH···O) (6)
143		140 s		0.45	0.28	υ(O···H) (28), $\omega(NH_2)_g$ (25), $\omega(C_{11}O_{16}H_{17}H_{21})$ (12), $\tau(C_{19}N_{18})$ (6), δ(CO···H) (6)
110		112 s		0	0.45	τ_{out} (CCCC) (29), $\omega(C_{11}C_1CC)$ (16), ω(CH) (15), υ(O···H) (9), τ_{in} (CCCC) (8), $\tau(C_{11}O_{16})$ (5)
92				0.13	0.5	υ(O···H) (43), δ(NH···O) (13), $\omega(C_{11}O_{16}H_{17}H_{21})$ (12), τ(O···HNC) (8), $\tau(N_{20}C_{19})$ (7)

(*continued on next page*)

Table 5 (*continued*)

Scaled[a]	FT-IR	FT-Raman	Mode	IR intensity[b] (KM/Mole)	Raman Intensity[c] (Å^4/AMU)	Assignment of each mode with PED in %
71		79 s		0.33	0.66	τ($C_{19}N_{18}$) (17), τ(C_1C_{11}) (14), υ(O···H) (14), δ(CO···H) (13), ω(NH_2)$_g$ (10), τ(O···HNC) (9)
29				0.67	1.57	υ(O···H) (32), ω($C_{11}O_{16}H_{17}H_{21}$) (18), ω(NH_2)$_g$ (18), τ($C_{19}N_{18}$) (8)
23				0.43	1.03	δ(CO···H) (31), ω($C_{11}O_{16}H_{17}H_{21}$) (17), τ($C_{11}O_{16}$) (15), υ(O···H) (11), δ(NH···O) (8)
8				0.23	1.63	υ(O···H) (38), δ(CO···H) (26), δ(NH···O) (12)

ν: stretching, γ:scissoring, ω: wagging, τ: torsion, ρ: rocking, Γ: twisting, β: in-plane bending, δ: out-of plane bending, Rbr: ring breathing, s: symmetric, as: antisymmetric, vs: very strong, s: strong, ms: medium strong, vw: very weak, w: weak, ug: unperturbed amino group of guanidinium, g: guanidinium, p: puckering, in: in-plane, out: out-of-plane, ring: benzene ring.

[a] The wavenumbers obtained at B3LYP/6-311G(d) level were scaled using NCA based on SQM Force field calculations.

[b] Relative IR absorption intensities normalized with the highest peak absorption equal to 100.

[c] Relative Raman activities normalized to 100.

are expected in the regions 1300-1000 cm^{-1} and 1000-675 cm^{-1}, respectively. The PED result revels that in-plane CCH bending modes were strongly coupled with ring stretching. The in-plane bending modes 19a, 8b and 14 were theoretically obtained with the PED contributions of 54% at 1520 cm^{-1}, 42% at 1446 cm^{-1}, 66% at 1331 cm^{-1}, corresponding modes observed in IR bands at 1520, 1428, 1395 cm^{-1} and weak Raman bands at 1454, 1410 cm^{-1} respectively. The medium bands observed in the IR spectrum at 810 cm^{-1} and 789 cm^{-1} and its counterpart Raman band at 855 cm^{-1} are attributed to the CH wagging modes. According to the DFT calculation, the bands associated with the wagging vibrations of the CH bonds are found to be at 851 cm^{-1} with PED of 48%, 814 cm^{-1} with PED of 98%, 790 cm^{-1} with PED of 18%. The out-of-plane CH bending corresponds to modes 10b, 10a and 11 respectively which have been identified as weak bands at 851 cm^{-1}, 814 cm^{-1} and 790 cm^{-1} in the experimental spectrum.

The carbon-carbon ring stretching vibrations usually occur in the region 1620-1280 cm^{-1} [74]. The strong band observed in IR at 1618 cm^{-1} and the weak band in the Raman spectrum at 1616 cm^{-1} can be assigned to the CC stretching mode 8a of G4AB. The wavenumber corresponding to the mode 8b is found to be at 1428 cm^{-1} in IR and 1454 cm^{-1} in Raman spectrum. The wavenumber corresponding to 19a mode of G4AB is identified at 1520 cm^{-1} in IR spectrum. The strong band observed in IR spectrum at 1395 cm^{-1} can be assigned to mode 14 of G4AB. The DFT calculations predicted the normal vibrations of the CC stretching modes 8a, 8b, 19a, and 14 at 1613 cm^{-1}, 1446 cm^{-1}, 1520 cm^{-1} and 1331 cm^{-1}, respectively, for disubstituted benzene ring of G4AB. The bands observed in the IR spectrum at 3489 cm^{-1} and 3395 cm^{-1} are attributed to the asymmetric and symmetric stretching modes, respectively, of the ring substituted amino group and corresponding Raman bands were absent in the spectrum. The calculated wavenumbers for these modes were predicted with PED contributions of 100% at 3488 cm^{-1} and 100% at 3398 cm^{-1}. The observed intensity and sharpness of the IR bands for these bands indicate the non-involvement of the NH_2 group in H-bonding in the solid as well as the gas phases of G4AB. The scissoring mode of the amino group is calculated to be a pure mode which is obtained at 1700 cm^{-1} with PED of 95%. The rocking mode of NH_2 group is expected in the region 1100-1000 cm^{-1} [73]. The medium strong bands observed in IR and Raman spectra at 1138 cm^{-1} are attributed to the rocking modes of the amino group. The normal co-ordinate analysis gives the band position of these modes at 1137 cm^{-1} with PED of 21% and at 1076 cm^{-1} with PED of 33%. The bands related to the wagging vibrations of the amino group are identified as medium strong bands in the IR spectrum at 640 cm^{-1} and Raman band at 642 cm^{-1}.

The asymmetric and symmetric stretching vibrations of the carboxylate group are expected in the regions 1600-1540 cm^{-1} and 1300-1100 cm^{-1}, respectively. In G4AB, the asymmetric stretching mode of the carboxylate group was inactive in the IR spectrum and also the Raman counterpart was observed with very weak intensity at 1730 cm^{-1}, whereas in the case of symmetric stretching mode, the IR band is active which was observed as medium strong band at 1121 cm^{-1} and the corresponding band was inactive in the Raman spectrum. The DFT calculations give very small PED contributions for the asymmetric and symmetric stretching modes of the carboxylate group which were calculated to be at 1731 cm^{-1} with the PED of 11% and at 1127 cm^{-1} with the PED of 16%, respectively. This is due to the involvement of H-bonding interactions with the neighbouring amino group in guanidinium cation and also due to the strong π-conjugation and n→π* hyperconjugation within the carboxylate group. The Raman spectrum shows a weak band at 1553 cm^{-1} for the stretching modes of the non-hydrogen bonded $C_{11} = O_{15}$ bond and a related IR band observed as a strong band at 1583 cm^{-1}. PED gives the contributions of the stretching vibrations of the $C_{11} = O_{15}$ bond at 1553 with 53%. The stretching vibrational mode of the hydrogen bonded $C_{11} = O_{16}$ bond of the carboxylate group is identified as very strong bands with high intensity in both the IR and the Raman spectra at 1375 cm^{-1}.

5. Conclusion

The G4AB crystal was successfully grown by slow evaporation technique. The dielectric permittivity and dielectric modulus reveal the behaviour of a single relaxation that is observed in the crystal. The presence of grain and grain boundary was studied using complex impedance spectra. The low dielectric constant value of the crystal has been established by the dielectric study and high thermal stability shows the possibility of crystal in photonic laser experiments and NLO device applications. The red shifted NH stretching wavenumbers and the broadening of corresponding bands in the solid state as well as the gas phase spectra, optimized molecular geometry and NBO analysis have confirmed the presence of N-H···O hydrogen bonding in G4AB. Due to the combined effect of n→π*, n→σ*, σ→σ* and π→π* the amounts of charge transferred increase with increasing binding energy. Similarly, the electron densities at the respective bond critical points vary fairly linearly with the strength of interaction, while their Laplacians also show a general increase with the binding energy. The total dipole moment, isotropic mean polarizability, anisotropic polarizability, static and dynamic first & second hyperpolarizabilies for the isolated gas phase molecule of G4AB were theoretically calculated and were compared with those values of similar NLO active organic molecules. The third order nonlinear optical property extensively studied by z-scan technique revealed high third order nonlinearity in the form of self-defocusing, two-photon absorption with saturable absorption. The calculated values of the HOMO-LUMO energy gap and the NLO response properties suggested the superior nonlinear optical activity of the molecule. The correlation between the nonlinear optical and dielectric properties was established.

Declaration of interests

The authors declare that they have no known competing financial

interests or personal relationships that could have appeared to influence the work reported in this paper.

Acknowledgments

D.S. thanks the Science Kerala State Council of Science, Technology and Environment Sasthra Bhavan, Pattom (P.O), Thiruvananthapuram – 695004, Kerala (KSCSTE), for the financial support (No. 002/SRPS/2014/CSTE dated 19-05- 2015). The authors (DS and LKJ) also acknowledge the DST-FIST program (SR/FST/College-182/2013, November 2013 & FIST No.393 dated 25-09-2014) to the Bishop Moore College Mavelikara for providing the UV visible, and workstation for computational work and measurements facilities. The author (DS) thank Science and Engineering Research Board, Department of Science and Technology, Government of India (DST SERB), New Delhi-110 070, for the financial support (SR/FTP/PS- 220/2012) for FT-IR measurement facilities. The author (DS) is highly grateful to Prof. T. Sundius for the Molvib program and fruitful discussions on the Normal Coordinate Analysis (NCA).

Appendix A. Supplementary data

Supplementary data to this article can be found online at https://doi.org/10.1016/j.optmat.2019.01.006.

References

[1] Zbigniew R. Grabowski, Krystyna Rotkiewicz, Chem. Rev. 103 (10) (2003) 3899–4032.
[2] P. Srinivasan, T. Kanagasekaran, R. Gopalakrishnan, J. Cryst. Growth 8 (2008) 2340–2345.
[3] Pedro S. Pereira Silva, Cláudia Cardoso, Manuela Ramos Silva, José A. Paixão, Ana Matos Beja, Maria Helena Garcia, Nelson Lopes, J. Phys. Chem. A 114 (7) (2010) 2607–2617.
[4] J. Zyss, J. Pecaut, J.P. Levy, R. Masse, Acta Crystallogr. Sect. B 49 (1993) 334–342.
[5] A. Suvitha, P. Murugakoothan, Spectrochim. Acta, Part A 86 (2012) 266–270.
[6] G. Saravana Kumar, P. Murugakoothan, Spectrochim. Acta, Part A 131 (2014) 17–21.
[7] E.S. Mansueto, C.A. Wight, J. Am. Chem. Soc. 111 (1989) 1900–1901.
[8] Z.B. Maksić, B. Kovačević, J. Phys. Chem. A 102 (1998) 7324.
[9] Z.B. Maksić, B. Kovačević, J. Phys. Chem. A 103 (1999) 6678.
[10] Z.B. Maksić, Z. Glasovac, I. Petanjek, J. Phys. Org. Chem. 15 (2002) 499.
[11] Graham Smith, Daniel E. Lynch, Karl A. Byriel, Colin H.L. Kennard, J. Chem. Crystallogr. 27 (1997) 307–317.
[12] Pedro S. Pereira Silva, Mauro A. Pereira Gonçalves, Manuela Ramos Silva, Anna Zawadzka, Bouchta Sahraoui, José A. Paixão, Opt. Mater. 84 (2018) 606–613.
[13] Pedro S. Pereira Silva, M.A. Pereira Gonçalves, Manuela Ramos Silva, A. Paixão José, Spectrochim. Acta Part A 172 (2017) 156–162.
[14] T. Uma Devi, A. Josephine Prabha, R. Meenakshi, G. Kalpana, C. Surendra Dilip, J. Mol. Struct. 1130 (2017) 472–479.
[15] P. Muthuraja, T. Joselin Beaula, T. Shanmugavadivu, V. Bena Jothy, M. Dhandapani, J. Mol. Struct. 1137 (2017) 649–662.
[16] Li Li, Daofeng Sun, Zhengping Wang, Xinyu Song, Sixiu Sun, Solid *State* Mater. Sci. 11 (2009) 1040–1043.
[17] G. Shanmugam, K. Ravi Kumar, B. Sridhar, S. Brahadeeswaran, Mater. Res. Bull. 47 (2012) 2315–2323.
[18] T.P. Srinivasan, S. Anandhi, R. Gopalakrishnan, Spectrochim. Acta, Part A 75 (2010) 1223–1227.
[19] E.J. Liang, C. Engert, W. Kiefer, Vib. Spectrosc. 6 (1993) 79–85.
[20] S. Nandhini, K. Sudhakar, S. Muniyappan, P. Murugakoothan, Opt. Laser Technol. 105 (2018) 249–256.
[21] P. Karuppasamy, Pandian Muthu Senthil, P. Ramasamy, S.K. Das, Optik 156 (2018) 707–719.
[22] J. Marek Drozd, Mol. Struct. 1155 (2018) 776–788.
[23] Paavai Era, R.O.M.U. Jauhar, G. Vinitha, P. Murugakoothan, Opt. Laser Technol. 101 (2018) 127–137.
[24] M. Drozd, Mater. Sci. Eng. B 136 (2007) 20–28.
[25] M. Drozd, Spectrochim. Acta, Part A 65 (2006) 1069–1086.
[26] J. Binoy, C. James, I. Hubert Joe, V.S. Jayakumar, J. Mol. Struct. 784 (2006) 32–46.
[27] Teodora Todorova, Oliver Kröcher, Delley Bernard, J. Mol. Struct. 907 (2009) 16–21.
[28] V. Sasikala, D. Sajan, K. Job Sabu, T. Arumanayagam, P. Murugakoothan, Spectrochim. Acta, Part A 139 (2015) 555–572.
[29] M. Drozd, D. Dudzic, Spectrochim. Acta, Part A 138 (2015) 539–549.
[30] D. Sajan, N. Vijayan, K. Safakath, Reji Philip, M. Karabacak, Spectrochim. Acta, Part A 108 (2013) 197–210.
[31] A. Longarte, J.A. Fernández, I. Unamuno, F. Castaño, Chem. Phys. Lett. 308 (1999) 516–522.
[32] E.D. Glendening, A.E. Reed, J.E. Carpenter, F. Weinhold, NBO Version 3.1. TCI, University of Wisconsin, Madison, 1998.
[33] A.D. Becke, Density-functional exchange-energy approximation with correct asymptotic-behaviour, Phys. Rev. A 38 (6) (1988) 3098–3100.
[34] C.T. Lee, W.T. Yang, R.G. Parr, Development of the Colle-Salvetti correlation-energy formula into a functional of the electron-density, Phys. Rev. B 37 (2) (1988) 785–789.
[35] M.J. Frisch, G.W. Trucks, H.B. Schlegel, G.E. Scuseria, M.A. Robb, J.R. Cheeseman, G. Scalmani, V. Barone, B. Mennucci, G.A. Petersson, et al., Gaussian 09, Revision C.01, Gaussian, Inc., Wallingford CT, 2009.
[36] T. Sundius, J. Mol. Struct. 218 (1990) 321–326.
[37] T. Sundius, J. Mol. Struct. 218 (1990) 321–326.
[38] T. Sundius, Vib. Spectrosc. 29 (2002) 89.
[39] T. Keith, AIMALL (Version 13.02.26), Tk Gristmill software, 2012.
[40] T. Arumanayagam, P. Murugakoothan, Mater. Lett. 65 (2011) 2748–2750.
[41] B.S. Benila, K.C. Bright, S. Mary Delphine, Opt. Quant. Electron. 50 (2018) 202.
[42] K. Boopathi, P. Rajesh, P. Ramasamy, Mater. Res. Bull. 47 (2012) 2299–2305.
[43] A.A. Attia, M.A.M. Seyam, S.S. Nemr, J. Mater. Sci. Mater. Electron. 29 (2018) 7325.
[44] B. Fall, A. Jalil, M. Gau, Ionics 24 (2018) 343.
[45] Hafiz Muhammad Tahir Farid, Ishtiaq Ahmad, Irshad Ali, Shahid M. Ramay, Asif Mahmood, G. Murtaza, Magn. Magn. Mater. 434 (2017) 143–150.
[46] Sameh Guidara, Habib Feki, Younes Abid, J. Alloy Comp. 663 (2016) 424–429.
[47] Shao Dong, Le Shi, a Lei Yin, Bao-Lin Wang, Zhen-Xing Wang, Yi-Quan Zhang, Xin-Yi Wang, Chem. Sci. 9 (2018) 7986–7991.
[48] R. Surekha, P. Sagayaraj, K. Ambujam, Opt. Mater. 85 (2018) 133–137.
[49] A. Saranraj, J. Thirupathy, S. Sahaya Jude Dhas, M. Jose, G. Vinitha, S.A. Martin Britto Dhas, Appl. Phys. B 124 (2018) 97.
[50] P. Vivek, P. Murugakoothan, Opt. Laser Technol. 49 (2013) 288–295.
[51] P.S. Pereira Silva, M. Ramos Silva, J.A. Paixão, A. Matos Beja, Acta Cryst. E 66 (2010) o524.
[52] E.M. Sheik-Bahae, A.A. Said, E.W. Van, Stryland, Opt. Lett. 14 (1989) 955–957.
[53] G. Vinitha, A. Ramalingam, J. Laser Phys. 18 (2008) 1070–1073.
[54] K. Thirupugalmani, S. Karthick, G. Shanmugam, V. Kannan, B. Sridhar, K. Nehru, S. Brahadeeswaran, Opt. Mater. 49 (2015) 158–170.
[55] Jesby George, D. Sajan, Alex Javeesh, Arun Aravind, G. Vinitha, R. Chitra, Opt. Laser Technol. 105 (2018) 207–220.
[56] Ireneusz W. Bulik, Robert Zale_sny, Wojciech Bartkowiak, Josep M. Luis, Bernard Kirtman, Gustavo E. Scuseria, Aggelos Avramopoulos, Heribert Reis, G. Manthos, J. Papadopoulos, Comput. Chem. 34 (2013) 1775–1784.
[57] Frédéric Castet, Benoît Champagne, J. Chem. Theor. Comput. 8 (2012) 2044–2052.
[58] Pedro S. Pereira da Silva, Pablo Martin-Ramos, Sergio R. Domingos, Maria do Carmo Bota de Sousa, Claudia T. Arranja, Abilio J.F.N. Sobral, Manuela Ramos Silva, ChemPhysChem 19 (2018) 82–92.
[59] Lewis E. Johnson, Larry R. Dalton, Bruce H. Robinson, Acc. Chem. Res. 47 (2014) 3258–3265.
[60] Tomasz Seidler, Katarzyna Stadnicka, Benoît Champagne, J. Chem. Theor. Comput. 10 (2014) 2114–2124.
[61] V. Sivasubramani, Jesby George, M Senthil Pandian, Ramasamy Perumalsamy, K. K Maurya, P. Pounraj, D. Sajan, New J. Chem. 42 (2018) 4261–4277.
[62] Marek Drozd, Dudzic Damian, Spectrochim. Acta, Part A 89 (2012) 243–251.
[63] R. Hutchison, M.A. Ratner, T.J. Marks, J. Am. Chem. Soc. 217 (2005) 2339–2350.
[64] Chang-Guo Zhan, Jeffrey A. Nichols, David A. Dixon, J. Phys. Chem. A 107 (2003) 4184–4195.
[65] E. Espinosa, E. Molins, C. Lecomte, Chem. Phys. Lett. 285 (1998) 170.
[66] G. Socrates, Infrared and Raman Characteristic Group Frequencies. Tables and Charts, third ed., Wiley, Chichester, 2001.
[67] N.B. Colthup, L.H. Daly, S.E. Wiberley, Introduction to Infrared and Raman Spectroscopy, third ed., Academic Press, New York, 1990.
[68] W.D. Kumler, J. Am. Chem. Soc. 76 (1954) 814.
[69] M. Drozd, J. Mol. Struct. 756 (2005) 173–184.
[70] G.P. Sheeja Mol, D. Aruldhas, I. Hubert Joe, S. Balachandran, A. Ronaldo Anuf, Jesby George, J. Mol. Struct. 1176 (2019) 226–237.
[71] G. Varsanyi, S. Szőke, Vibrational Spectra of Benzene Derivatives, Academic Press, New York and London, 1969.
[72] N.P.G. Roeges, A Guide to the Complete Interpretation of Infrared Spectra of Organic Structures, Wiley, New York, 1994.
[73] G. Varsanyi, Assignments for Vibrational Spectra of Seven Hundred Benzene Derivatives, Hilger, London, 1974.
[74] D. Lin-Vien, N.B. Colthup, W.G. Fateley, J.G. Graselli, The Hand Book of Infrared and Raman Characteristic Frequencies of Organic Molecules, Academic Press, New York, 1991.